https://doi.org/10.5194/egusphere-2026-5057
Preprint. Discussion started: 8 September 2026
© Author(s) 2026. CC BY 4.0 License.

GNSS Reflectometry on the McMurdo Ice Shelf

Seebany Datta-Barua[1], Alison F. Banwell[2,3], Jonah Wilkes[1], Alec Weedman[1], Roohollah Parvizi[1], Christian Allen[1], Aiden Verdin[1], Hiroki Kawai[1], Logan Garcia[1], and Kristine M. Larson[4]

[1]Illinois Institute of Technology, Mechanical, Materials and Aerospace Engineering Department, 10 W. 32nd St., RE-243, Chicago, IL 60616, USA
[2]Cooperative Institute for Research in Environmental Sciences (CIRES), University of Colorado Boulder, Boulder, CO 80309, USA
[3]Centre for Polar Observation and Modelling (CPOM), School of Geography and Natural Sciences, Northumbria University, Newcastle Upon Tyne, UK
[4]Department of Aerospace Engineering Sciences, University of Colorado Boulder, Boulder, CO, USA

Correspondence: Seebany Datta-Barua (sdattaba@illinoistech.edu)

Abstract. The ability to monitor glaciated surface types, including snow, ice and meltwater, at a high spatial resolution, is critical for monitoring overall glacier mass balance. Using an Antarctic ice shelf as a study site, we tested the feasibility of Global Navigation Satellite System reflectometry (GNSS-R) and GNSS interferometric reflectometry (GNSS-IR) in monitoring glacier surfaces. During the 2023-24 Antarctic austral summer, we conducted a field campaign to collect GNSS-R front-end samples from one 9-m tower and GNSS-IR samples from one 1.5-m tower offset 14 m away horizontally, at each of two sites located on the McMurdo Ice Shelf near McMurdo Station, Antarctica. The towers near Phoenix airfield were on snow-covered ice. The towers near McMurdo's former Pegasus airfield were on a heterogeneous surface of bare ice and snow-covered ice, which varied temporally. From mid-November to early December 2023, we collected GNSS-R, GNSS-IR, camera imagery, and data of the glacier surface within a 20 m radius at each of the two 9-m tower sites. All data were returned to the lab for post-processing.

We show our results processing the GNSS-R front-end samples to estimate the surface reflectivity from the signal-to-noise ratio. We find that the GNSS-R signal-to-noise ratio is insufficiently strong for estimating surface reflectivity. We also show our results processing the Earthscope geodetic receiver data for interferometric reflectometry, looking at the spectral peak amplitude as the indicator of surface type. We find that the GNSS-IR spectral peak amplitude mean and bias differ between the two sites, but cannot rule out the role that hardware differences between the sites may have in this.

1 Introduction

The cryosphere, including worldwide ice sheets and glaciers, is melting at an accelerating rate in response to Earth's warming climate (Hanna et al., 2020). Therefore, it is important to be able to monitor changing glaciated surface conditions, including

https://doi.org/10.5194/egusphere-2026-5057
Preprint. Discussion started: 8 September 2026
© Author(s) 2026. CC BY 4.0 License.

meltwater, as well as snow and ice-covered surfaces at high spatial resolutions, especially in order to better predict future rates of ice loss to the oceans. Antarctica is the Earth's largest ice sheet and could contribute up to 58 m of global sea-level rise if it were to melt completely. Ice shelves are the floating extensions of glaciers on land and surround about 75 percent of the Antarctic Ice Sheet (Fürst et al., 2 Ice shelves are important as they restrain glacier ice mass on land that would otherwise flow more rapidly into the ocean and contribute to global sea level rise. However, Antarctica's ice shelves are thinning in response to both surface melting from atmospheric convective heating and solar radiation, and basal melting due to warming ocean w n turn, this means that, as the Earth's climate warms, ice shelves are progressively weakening, diminishing their ability to hold back inland glacier ice (Fricker et al., 2025). Stress changes due to surface loading from melt pond development and drainage is also known to weaken and fracture ice shelves (Banwell et al., 2013, 2 024; Scambos et al., 2003, 2009).

Satellite-based remote sensing usually cannot resolve surface melting at a spatial or temporal resolution that is sufficiently high to be of interest, and satellite-derived surface melt can not usually be validated against , ground-based observations. GNSS reflectometry leverages signals from GNSS that have reflected off surfaces to remotely sense properties of the environment. Reflectometry is well-suited to an ice shelf, as this type of glacier is flat with open sky viewing conditions, in contrast to a mountain glacier, which will be sloped and often have nearby mountains obscuring satellite lines-of-sight.

Reflectometry, particularly GNSS interferometric reflectometry (GNSS-IR), has been used in a wide variety of contexts in Earth science, including to measure snow accumulation rates in glaciated regions (Larson, 2019). The method is also sensitive to firn density when used along with the GNSS-derived vertical position (Larson et al., 2015). The GNSS-IR method has been used for re-analyses of historic data, and has shown that surface heights in Antarctica can be accurately measured at about 2 cm over months and years (Siegfried et al., 2017; Shean et al., 2017). Most of these analyses are based on measuring the frequency at which the spectral peak occurs, which geometrically corresponds to the surface vertical distance below the antenna. Very few studies, if any, have leveraged the information content in the magnitude of the spectral peak. One of aims of this study is to examine whether spectral peak amplitude, a by-product of standard GNSS-IR processing, can serve as a passive indicator of surface type variability across azimuthal regions around deployed receivers.

Meanwhile, the possibility of surface ice melt monitoring using only the reflected GNSS signal non-interferometrically from a dedicated downward-pointing antenna was previously demonstrated on a lake surface. Henceforth in this work we use"GNSS reflectometry" or "GNSS-R" specifically for the non-interferometric form of sensing. In prior fieldwork, Parvizi et al. (2024) collected GNSS-R data over a heterogeneous ice-covered lake, which showed a moderate positive correlation between the GNSS signal-to-noise ratio (SNR) and georeferenced camera images of the mixed ice and water lake surface, with the camera image mean red pixel intensity within the GNSS signal-scattering zone used as a numerical discriminant between ice and water. However, to our knowledge, GNSS-R data have not previously been collected from a glaciated surface.

In this work, we asked: 1) how does the GNSS-R-based SNR respond to different surface types of an ice shelf? To address the question, for a temporally-varying, heterogeneously bare and snow-covered ice shelf, we compute the GNSS-R SNR for satellites. We also asked: 2) How does GNSS-IR spectral peak amplitude differ for differing ice shelf surface types? For this, we compare the GNSS-IR-derived spectral peak amplitude from the two sites.

https://doi.org/10.5194/egusphere-2026-5057
Preprint. Discussion started: 8 September 2026
© Author(s) 2026. CC BY 4.0 License.

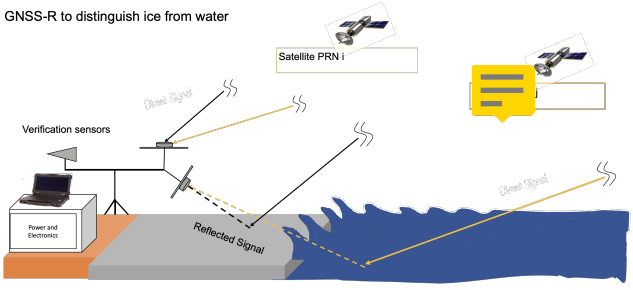


Figure 1. Illustration of the GNSS reflectometry (GNSS-R) concept. A downward-pointing antenna receives the GNSS signal after it has interacted with the surface being sensed.

2 BACKGROUND

Figure 1 illustrates the concept of having a dedicated antenna for GNSS-R. While a right-hand circularly polarized (RHCP) upward-facing antenna is used for positioning, a collocated downward-angled antenna of the opposite polarization of the GNSS signal is dedicated to collecting the signal after it has reflected off the surface. The single point at which the angle of incidence equals the angle of reflection is called the "specular point" (SP), but in general due to surface roughness, most energy will forward scatter from a region around the SP corresponding to the first Fresnel zone (FZ). Different surface types (e.g., ice and water in the cartoon) will scatter the signal differently, largely depending on surface roughness, compared to the wavelength of the signal being used. The measure of the signal-to-noise ratio SNR of the forward scattered signal is related to the surface reflectivity of the surface. The SNR is computed from the accumulated power at the correlation peak P_{max} searched over code delays and Doppler shifts, relative to the mean accumulation at the same Doppler shift for all delays beyond one chip on either side of the peak (Parvizi et al., 2024):

$$SNR = \frac{P_{max} - P_{noise}}{P_{noise}} \tag{1}$$

where P_{noise} is the average background level of the acquisition map beyond ± 1 chip of the main peak. The surface reflectivity is related to the SNR through a number of known or estimatable quantities as given by (Chew et al., 2018). The SNR may be computed from a GNSS r er, yielding a measure of the surface reflectivity. However, commercial receivers are not designed for this technique, and since the scattered signal is likely to be weak, collecting the front-end samples from the antenna with a universal software radio peripheral (USRP) and then post-processing them allows us to try various techniques to maximize the signal accumulated. While SNR and SR variations with surface were shown for a lake surface with versus without ice cover (Parvizi et al., 2024; Datta-Barua et al., 2025), our hypothesis in this work is that there should likewise be SNR variations reflecting from an ice shelf surface, especially when glacier ice is exposed (i.e. not covered by snow).

GNSS-IR refers to the use of a single right-hand circularly polarized antenna, receiving both the direct and the multipath signal (Fig. 2). For satellites at low elevation, the direct and multipath signals arrive as a superposition at the antenna. As the

https://doi.org/10.5194/egusphere-2026-5057
Preprint. Discussion started: 8 September 2026
© Author(s) 2026. CC BY 4.0 License.

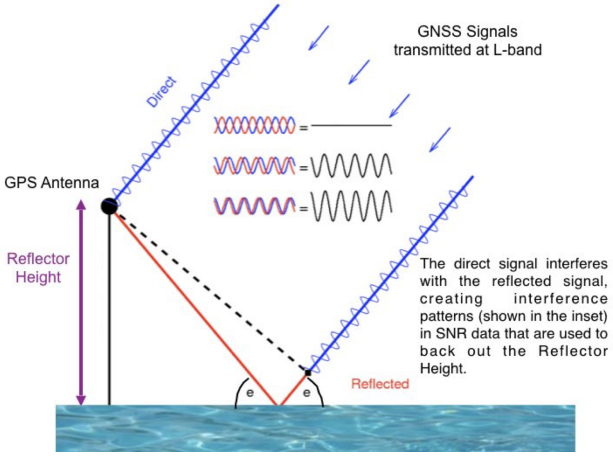


Figure 2. Principle of GNSS interferometric reflectometry (GNSS-IR) reprinted from (Larson, Accessed: 03 September 2024). The interference observed in the SNR time series is a function of elevation angle and reflector height.

satellite rises or sets, the signals will constructively or destructively interfere resulting in an elevation-dependent signal-to-noise ratio. The interference is a function of the reflector height H_R and satellite elevation angle el.

$$SNR(el) \quad = \quad A(el)\sin\left(\frac{4\pi H_R}{\lambda}\sin(el)+\phi\right) \tag{2}$$

A geodetic receiver with a 0° elevation mask can be used to collect the SNR for this purpose. A Lomb-Scargle periodogram of the SNR of a single line-of-sight rising or setting at low elevations, e.g., 5°-25°, can be used to estimate the reflector height. When combining the estimates from multiple lines-of-sight and estimating reflector height over days to months, GNSS-IR has been shown to be very useful for the ability to monitor tides from geodetic receivers in coastal areas, and for measuring snow accumulation on the ground surrounding a geodetic station Larson (2019).

The amplitude of the periodogram has not historically been used as much. The periodogram spectral peak amplitude is essentially a measure of the peak of the power spectral density and corresponds to the amount of signal power at the estimated reflector height. Signals scattered from a surface that is uneven over the path the Fresnel zone traverses as the satellite rises or sets will tend to lower the spectral peak amplitude and similarly the peak-to-noise ratio. The spectral peak and the peak-to-noise ratio are also a function of the surface type, as shown in examples by (L[illegible], Accessed: 03 September 2024).

3 DATA COLLECTION

The objective of this work is to collect GNSS signals after they have reflected off the ice shelf, under different glaciated surface conditions (including snow of various density, ice and meltwater), and to test whether the reflected signal properties derived from SNR vary with surface type. Two sites are selected, with differing surface types: one of snow-covered ice near the current Phoenix airfield, and heterogeneously snow-covered and bare ice at Pegasus, the former McMurdo airfield, which, since 2016,

https://doi.org/10.5194/egusphere-2026-5057
Preprint. Discussion started: 8 September 2026
© Author(s) 2026. CC BY 4.0 License.

has experienced too much surface melting for aircraft operations. Figure 3 inset shows the Antarctic continent with the U.S. base of Antarctic operations, McMurdo Station, labeled with a red star. McMurdo Station lies on Ross Island, in the Ross Sea. Part of the Ross Sea is covered by the Ross Ice Shelf, of which a small area near to McMurdo Station is known as the McMurdo Ice Shelf. The seashore adjacent to the McMurdo Ice Shelf is known as the McMurdo Sound and is periodically covered with sea ice, which breaks up (sometimes completely) in the Antarctic summer, unlike the ice shelf. The satellite image in Figure 3 labels McMurdo Station and the "ice shelf transition" between the seasonal sea ice and more permanent glacial ice shelf. Phoenix and Pegasus airfields are labeled on the map. Parallel straight segments in the ice to the left of the Pegasus airfield label and in the snow to the left of the Phoenix Airfield label indicate locations of the runways.

Red boxes label the approximate sites of the towers, sited next to the runways (Figure 3). As seen from the 10 m resolution Sentinel-2 satellite image, dated 9 Nov 2023, the two sites have generally different terrain. Phoenix is snow-covered ice shelf, and appears largely white or gray. Pegasus, on the other hand, is near a region of mostly bare ice, which appears blue because the ice absorbs red wavelengths more readily than blue ones. During the austral melt season from mid December to early February, the area near Pegasus airfield experiences significant surface melting relative to Phoenix airfield.

The two sites were selected for their difference in surface types due to varying local climate conditions. A second factor was the relative ease of access to both of these sites. A groomed road is maintained between McMurdo and Phoenix, which enables wheeled vehicle access to the Phoenix tower site. The route between Phoenix and Pegasus was not maintained in the 2023-24 field season, but was still flagged from prior years and accessible by tracked vehicle.

Each site was designed to have a GNSS-R tower near enough to a GNSS-IR tower to have common GNSS-R and -IR fields-of-view of the region of the surface between the towers. The goal was to compare the estimates of surface reflectivity and SNR between the two sites and between the two reflectometry methods. Tower sizing was estimated prior to fieldwork by simulation of satellite elevation angles, first Fresnel zone, and height of the antennas. As GNSS-R uses only reflected signals, the highest elevation satellites are targeted. Meanwhile GNSS-IR uses low-elevation satellites. With simulation via GPS almanacs, we sized a 9 m tower and 2 m tower about 14 m apart. At each site, two 9-meter (30 ft) towers were established before the field season. At Phoenix the 9-m tower was raised due south of the pre-existing 2-m GNSS antenna "PHNX" in operation by EarthScope for a number of years, since at this latitude most satellites would be in the northern part of the sky. At Pegasus the two towers were installed aligned east-west in order to have an alternative geometry in case the opposite tower blocked the signal to the satellites to the north.

Data were collected during the 2023-24 field season from mid-November to early-December. The antennas and sensors were mounted at Phoenix on the local day of 17 Nov 2023, and at Pegasus on 20 Nov 2023.

Figure 4 shows a schematic of the sensors used at each 9-m tower. At each site, the 9-m tower supports: one upward-facing RHCP GNSS antenna D_0 (for positioning), one downward-facing lefthand circularly polarized (LHCP) GNSS antenna for reflectometry, one lidar, and four cameras. The 9-m positioning antenna at Phoenix (PX10), at Pegasus (PG10) and at the 2-m tower at Pegasus (PG02) are each Trimble Zephyrs connected to a portable Trimble geodetic receiver with solar array mounted on the box lid. These receivers operate almost continuously for the entire period they are sited. Mounted just below the positioning antenna on each 9-m tower is the LHCP reflectometry antenna R_0. The signal from the positioning antenna is

https://doi.org/10.5194/egusphere-2026-5057
Preprint. Discussion started: 8 September 2026
© Author(s) 2026. CC BY 4.0 License.

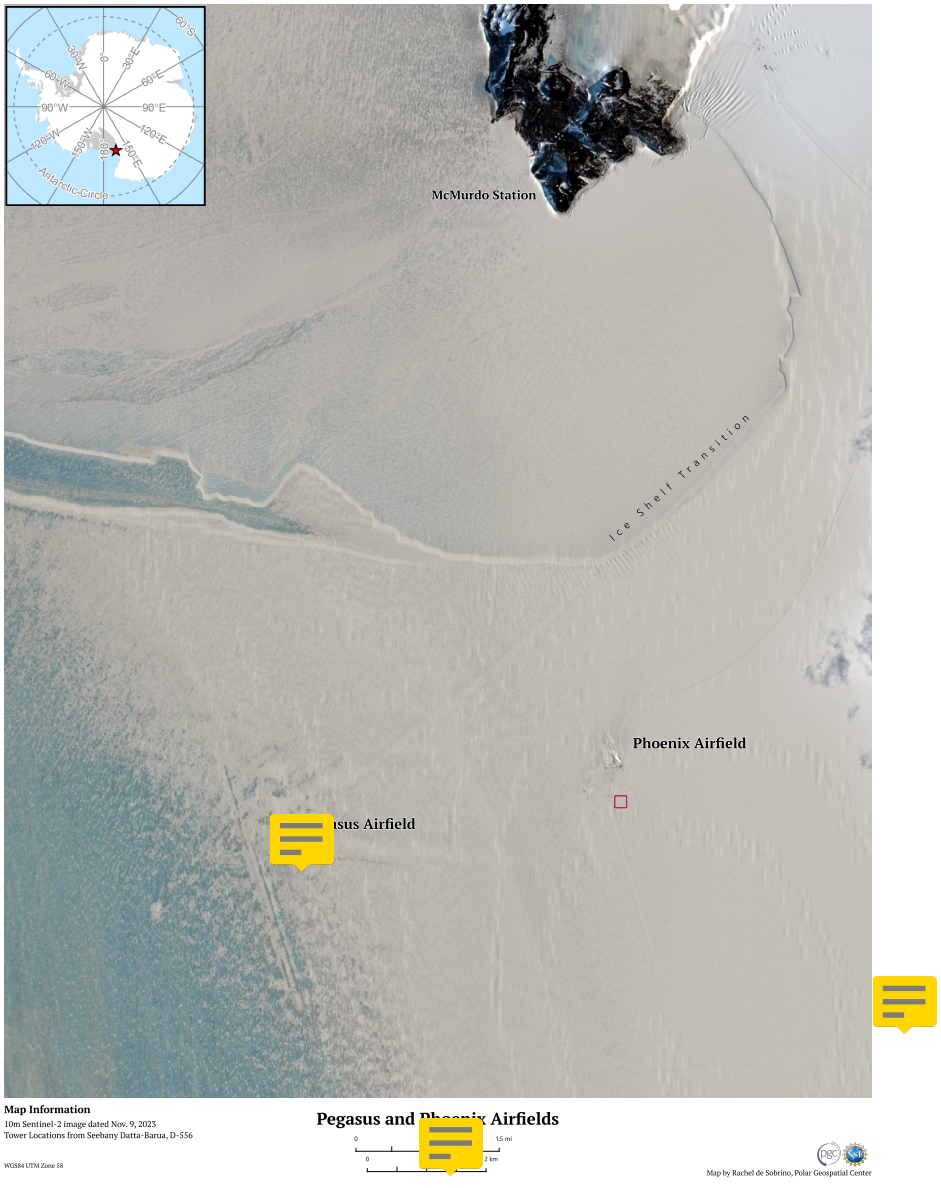


Figure 3. Sentinel-2 satellite image of the reflectometry field sites. Map by Rachel de Sobrino, Polar Geospatial Center. Phoenix site is at (77° 56' 53" S, 166° 44' 41.2" E). Pegasus site is at (77° 57' 23" S, 166° 30' 8" E). Inset: map of Antarctica and site of McMurdo Station and the McMurdo Ice Shelf is indicated by a red star.

split to drive the GPS-disciplined oscillator of the USRP that serves as the GNSS-R front-end. Closer to ground level, four IP security cameras are angled toward the ground to image the ground as near to the tower as about 3 m horizontally, and span about 300° azimuthal FOV around the tower. The area out of the cameras' FOV is the path by which we walked to and from the base of the tower at the time of data collection. A lidar is also mounted on the tower at each site at a height such that its lowest

https://doi.org/10.5194/egusphere-2026-5057
Preprint. Discussion started: 8 September 2026
© Author(s) 2026. CC BY 4.0 License.

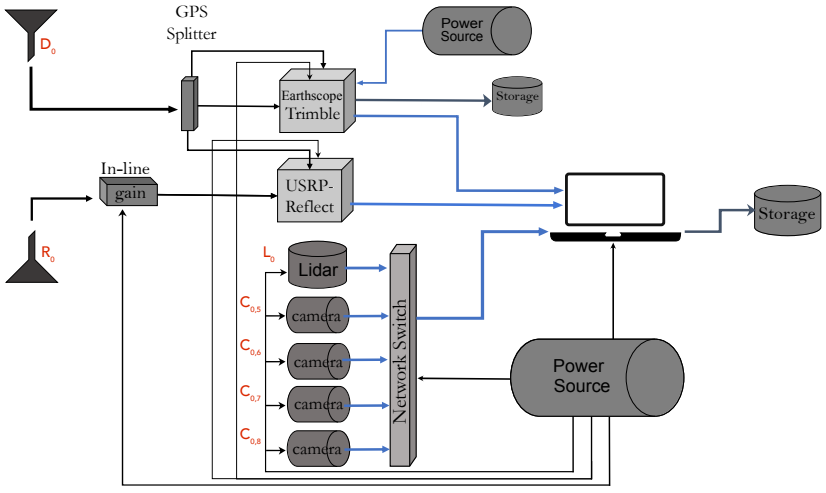


Figure 4. Schematic of the sensor suite at the Phoenix 9-m tower. The tower at Pegasus is identical except the cameras are identified as $C_{0,1}, C_{0,2}, C_{0,3}, C_{0,4}$.

elevation scan reaches about 3 m away from the tower. Prior simulation of reflection zones indicated that this is the closest any GNSS-R Fresnel zone will generally reach to the base of the tower.

Upon site setup, distances between instruments are measured and cameras are angled and recorded, as shown in the schematics in Fig. 5 for Phoenix and Fig. 6 for Pegasus. Each schematic shows a scale model of the relative positions of the 9-m and 2-m towers. The 2-m tower hosts one upward-facing RHCP GNSS antenna I_0 (used for both positioning and GNSS-IR). The pre-existing Phoenix site PHNX has a Septentrio PolaNt-x-MF connected to a Septentrio Polarx5 geodetic receiver (courtesy of EarthScope) and powered by a solar array facing north to maximize sunlight. The lidar L_0 at Phoenix is a Velodyne VLP-16 whose manufacturer-defined body axes $\hat{x}_L, \hat{y}_L, \hat{z}_L$ align with a transverse-boom-up coordinate system $\hat{t}, \hat{b}, \hat{u}$ that is used to define positions of sensors. The lidar at Pegasus is an Ouster OS0-32 whose body coordinates are given by $\hat{x}_L = -\hat{b}, \hat{y}_L = \hat{t}, \hat{z}_L = \hat{u}$ at that site.

Figure 7 shows a photo of the Phoenix site. The surface consists of relatively dense, windblown snow. The 9-m tower is on the right. Near the base of the left guy wires from this 9-m tower, the pre-existing PHNX 2-m tower is visible. Its solar array appears as the two dark rectangles near the base of the tall tower. The perimeter around the data collection zone is flagged to prevent excessive disturbance of the site. A weather station (tower at left, with a wind vane at the top) was within the perimeter of the Phoenix site as well. This was unintentional and instead due to the fact that the pre-existing 2-m tower and

https://doi.org/10.5194/egusphere-2026-5057
Preprint. Discussion started: 8 September 2026
© Author(s) 2026. CC BY 4.0 License.

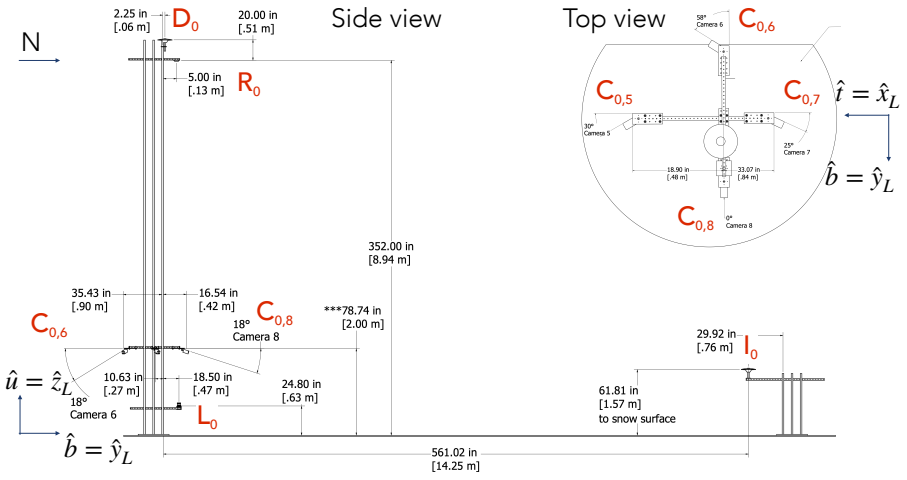


Figure 5. Left and bottom: scale model of the Phoenix 9-m tower at left and 2-m tower at lower right. Top right: top-down view of the 9-m tower. Sensor origins are labeled in red, dimensions and angles are recorded as measured on-site.

weather station were already there, and we wished to site the 9-m tower so that the GNSS-R and GNSS-IR antennas would have overlapping FOVs.

Figure 8 shows the Pegasus site. At this site the GNSS-IR antenna was mounted at a similar height to the existing GNSS-IR tower at the other site, PHNX. Since the receiver PHNX had been installed years before, with the snow accumulation, the tower had been partially buried such that the antenna was only about 1.6 m above the surface. We sought to match that height at Pegasus. After being initially mounted on 20 Nov 2023 at about 1.8 m above the ice, on 23 November 2023 before the first GNSS-R data collection we lowered the PG02 antenna and moved it horizontally further away from the tower. This meant the antenna I_0 was not mounted at the top of the tower, but on a boom 1.6 m above the surface, so a section of the tower extended above the PGSS-IR antenna.

While the GNSS-R antenna, lidar, and cameras were affixed to the 9-m towers at each site for the duration of our field season (about 4 weeks), they were only powered on while we were on-site with a portable generator, an electronics box containing the USRP to collect front-end samples and supporting communication electronics, and a laptop and external storage device, all of which we transported for data collection each day of fieldwork. At the field site, we temporarily disconnected the 9-m positioning antenna from the Earthscope receiver port to connect it into a splitter that feeds the signal back to the Earthscope

https://doi.org/10.5194/egusphere-2026-5057
Preprint. Discussion started: 8 September 2026
© Author(s) 2026. CC BY 4.0 License.

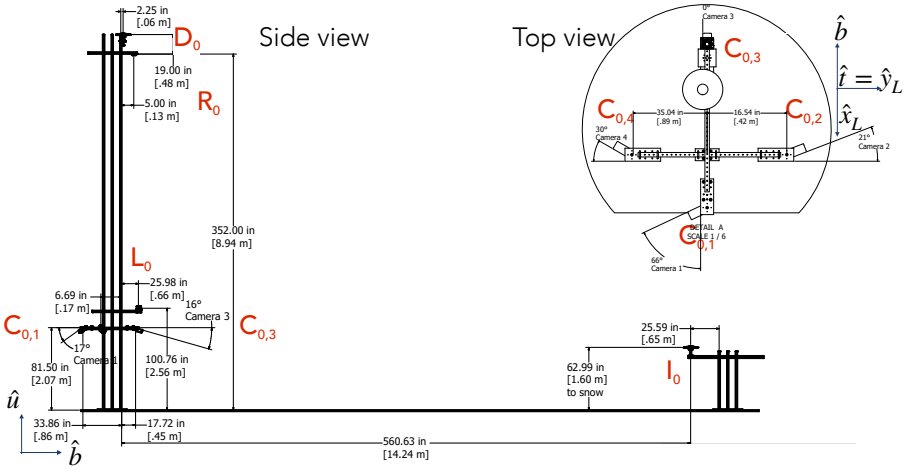


Figure 6. Left and bottom: scale model of the Pegasus 9-m tower at left and 2-m tower at lower right. The 9-m tower configuration is for data collected on and after 23 November 2023. Top right: top-down view of the 9-m tower. Sensor origins are labeled in red, dimensions and angles are recorded as measured on-site.

receiver but also to the GPS-disciplined oscillator on our USRP. The purpose is to have the oscillator in the USRP that sets the timing for sampling, driven by a GPS-timed signal.

After connecting all remaining instruments to the electronics box and powering them on, a python script initiated data collection from all sensors. The scripts created one text logfile for the each of the USRP, lidar, and cameras, noting the local time at the end of data collection and duration of the process. Data were collected in multiple parts, each initiated by one run of the data collection script (called a "part"), alternatingly one-minute or an hour. We generally collected data in 1-minute segments, to ensure a communication connection to all instruments was operating, alternating with 60-minute segments of data collection. At the end of data collection, the electronics box was powered down, the cameras, lidar, GNSS-R antenna disconnected, and the Earthscope antenna cable D_0 disconnected from the splitter and reconnected to the Earthscope chassis to resume geodetic data collection. This process would take about 15 minutes, so the rinex files from the positioning antennas at each site, will have data discontinuities of a few minutes sometime within the hour before the first data collection part and again within about 15 minutes after the end of the last part.

The USRP collected about 1 GB per minute in binary format, the Velodyne lidar at PHNX 70 MB/min in .pcap format, the Ouster lidar at PGSS 300 MB/min in .pcapng plus a .json lidar parameter file of a few kB, and cameras collected tens of MB

https://doi.org/10.5194/egusphere-2026-5057
Preprint. Discussion started: 8 September 2026
© Author(s) 2026. CC BY 4.0 License.



Figure 7. Photo of experimental field site at Phoenix airfield. The 9-m tower is visible on the right, with the rectangular solar panels of PHNX receiver just to the left of it. The leftmost tower is a weather station and is not part of the experiment but lies within a 15-m radius that is marked off with pole-mounted flags to limit traffic within the field of view. The terrain is wind-blown snow.

per minute in mp4 format. Each hour of data collected yields a 72 GB GNSS-R binary file; lidar pcap file on the order of a few GB; and camera video files each on the order of about 1 GB. These data were collected on a 500 GB solid state external drive dedicated to a given site (PGSS or PHNX). Upon returning to the lab each evening, they were copied redundantly to two 10 TB storage drives, and the 500 GB drives wiped empty for the next field use.

180 Tables 1-2 list the local dates and UT times for which data were collected at the Phoenix and Pegasus sites, respectively, derived from the logfiles. Local time at McMurdo Station was New Zealand Daylight Time, which is UTC + 13 h.

At Phoenix the lidar was initially mounted 2.34 m above the ground for data collected 19 November, but after taking into account the Velodyne lidar's elevation scanning range of 15 degrees below the lidar's body horizon, on 23 November we

https://doi.org/10.5194/egusphere-2026-5057
Preprint. Discussion started: 8 September 2026
© Author(s) 2026. CC BY 4.0 License.

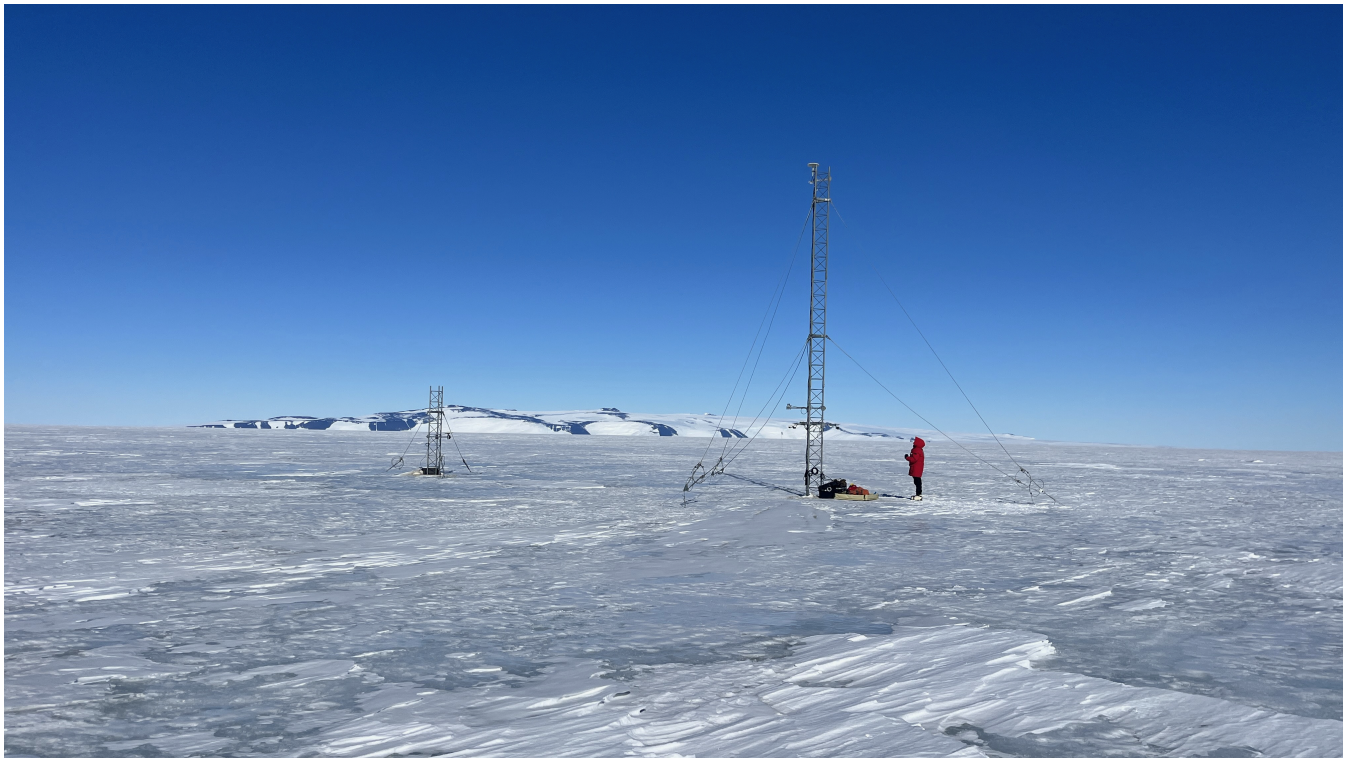


Figure 8. Photo of experimental field site at Pegasus. The 9-m tower is visible on the right, and the shorter tower on which the GNSS-IR antenna is mounted, at left. The terrain has patches of windblown snow on otherwise bare ice.

remounted it closer to the ground in order to have the lidar scan the surface within the desired field of view of the cameras. At Phoenix, partway during the field season, e.g., 27 November, part 2, camera 7 would occasionally stop collecting data during a long data part and cause the python script to stop running. While its data file was closed out and readable, the remaining camera files were not, nor were logfiles output at the completion of the script. For this reason, some parts' duration are not extractable from the logfiles, and while camera files exist, they are marked with a "∼" to denote that they are not readable mp4 in a standard video player without repairing. We attempted shorter data collection durations: 27 Nov part 5 of 20 minutes correctly executed and exited, but 5 Dec part 5 of duration 30 minutes did not. Therefore, starting 2 December part 6, we would in the alternating parts include one minute of all four cameras' data, followed by one part of longer duration with only cameras 5, 6 and 8 (plus the lidar and USRP, which were unaffected). For this reason camera 7 data are shut off for 60-minute data collection durations in December.

We note that the PHNX data (parts 1–5) collected on 8 December should be excluded from further analysis. During field operations on this date, we observed that the GNSS-R gain cable had become disconnected from the USRP. Furthermore, these data closely resemble laboratory measurements acquired using the USRP alone, whereas data collected on all other dates, parts, and sites are mutually consistent and distinct from the laboratory noise measurements. We therefore attribute the anomalous

https://doi.org/10.5194/egusphere-2026-5057
Preprint. Discussion started: 8 September 2026
© Author(s) 2026. CC BY 4.0 License.

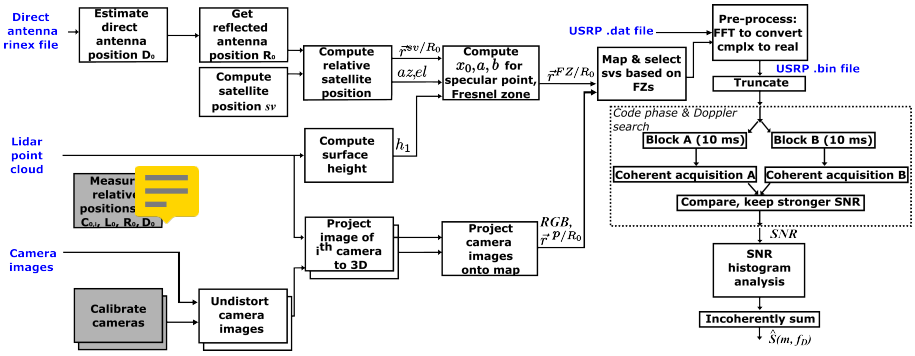


Figure 9. GNSS-R processing flowchart. Blue text identifies data files. Gray boxes identify calibration steps that are done offline.

measurements on 8 December to the disconnected gain cable, which was likely not fully secured prior to transport and became detached during transit.

At Pegasus, some of the cameras would sometimes still be collecting data after the other instruments had shut off. For these, we manually force quit, which left some of the log files available for computing start and end times (e.g., 8 Dec Part 4), or no logfiles were produced. In the cases where we force quit the data collection, the camera files exist but may not have terminated correctly, so appear as "∼" in the table and may need to be repaired before use.

The data collection configurations for Phoenix and Pegasus are each shown in Table 3. While approximate coordinates were obtained during field work, the position information for D_0, I_0 are ITRF2020/IGS20 reference frame estimates based on the rinex files for 20 November 2023 using the Canadian Geodetic Survey Precise Point Positioning service (Survey, Retrieved July 23, 2026). For camera orientation angles, the first number in a sum is the value that was measured in the field, and the second is an adjustment made manually when post-processing the data to align camera images with lidar point clouds.

The lidar and camera data collected in the field were randomly inspected at the McMurdo Station lab toward the end of the fieldwork for confirmation of data quality. The Ouster manufacturer provides python visualization software that were used to confirm the collection of lidar data on-site, but not for analysis. At the end of the fieldwork period, the EarthScope team processed the Trimble data and produced rinex files for our use. Due to the file size and lack of time in the field and processing capability, the USRP data were only examined after returning to the US.

4 GNSS-R ANALYSIS

4.1 METHOD

The processing workflow for the GNSS-R data in conjunction with the positioning receiver, cameras and lidar is shown in Fig. 9. The overall concept is to use the camera and lidar to map a top-down view of the surface, then to identify the Fresnel zones of GPS satellites that are in the sky, and to select those to focus on for computing the SNR via signal acquisition. Each

https://doi.org/10.5194/egusphere-2026-5057
Preprint. Discussion started: 8 September 2026
© Author(s) 2026. CC BY 4.0 License.

Table 1. DATA COLLECTION TIMES AT PHNX IN 2023

Local Date mm-dd	Part	Duration min	UT Start Time mm-dd HH:MM:SS	UT End Time mm-dd HH:MM:SS	USRP	lidar	Cam 5	Cam 6	Cam 7	Cam 8
11-19	1	20	11-19 02:18:17.78	11-19 02:19:03.68	✓	✓	✓	✓		✓
	2	5	11-19 03:14:26.29	11-19 03:19:33.16	✓	✓	✓	✓	✓	✓
	3	20	11-19 03:20:33.55	11-19 03:40:40.12	✓	✓	✓	✓	✓	✓
11-27	1	1	11-27 02:50:44.33	11-27 02:51:50.90	✓	✓	✓	✓	✓	✓
	2	n/a	No text file available.		✓	✓	∼	∼	✓	∼
	3	1	11-27 03:54:51.40	11-27 03:55:58.05	✓	✓	✓	✓	✓	✓
	4	n/a	No text file available.		✓	✓	∼	∼	✓	∼
	5	20	11-27 04:11:42.66	11-27 04:31:49.50	✓	✓	✓	✓	✓	✓
11-28	1	1	11-28 02:31:53.01	11-28 02:32:59.64	✓	✓	✓	✓	✓	✓
	2	1	11-28 02:35:07.94	11-28 02:36:14.52	✓	✓	✓	✓	✓	✓
	3	60	11-28 02:37:04.84	11-28 03:37:10.72	✓	✓	✓	✓	✓	✓
12-02	1	0	12-01 23:41:56.13	12-01 23:41:58.22		✓	✓	✓	✓	✓
	2	0	12-01 23:44:24.08	12-01 23:44:26.16		✓	✓	✓	✓	✓
	3	1	12-01 23:48:54.47	12-01 23:50:01.17	✓	✓	✓	✓	✓	✓
	4	n/a	No text file available.		✓	✓	∼	∼	✓	∼
	5	30	12-02 00:11:17.37	12-02 00:11:55.50	✓	✓	∼	∼	✓	∼
	6	30	12-02 01:03:45.12	12-02 01:33:50.97	✓	✓	✓	✓		✓
	7	1	12-02 01:39:12.81	12-02 01:40:34.39	✓	✓	✓	✓		✓
12-05	1	1	12-05 03:31:12.36	12-05 03:31:45.45	✓	✓	✓	✓		✓
	2	1	12-05 03:34:51.38	12-05 03:35:58.06	✓	✓	✓	✓	✓	✓
	3	n/a	No text file available.		✓	✓	∼	∼	✓	∼
	4	60	12-05 04:39:28.68	12-05 05:39:35.44	✓	✓	✓	✓		✓
12-08	1*	1	12-07 22:55:45.12	12-07 22:56:51.80	✓	✓	✓	✓	✓	✓
	2*	60	12-07 22:58:07.03	12-07 23:58:13.74	✓	✓	✓	✓		✓
	3*	1	12-08 00:01:50.10	12-08 00:02:56.66	✓	✓	✓	✓	✓	✓
	4*	60	12-08 00:04:26.79	12-08 01:04:33.52	✓	✓	✓	✓		✓
	5*	1	12-08 01:05:19.58	12-08 01:06:26.22	✓	✓	✓	✓	✓	✓
	6	1	12-08 01:26:35.60	12-08 01:27:42.16	✓	✓	✓	✓	✓	✓
	7	60	12-08 01:28:32.30	12-08 02:28:39.05	✓	✓	✓	✓		✓
	8	1	12-08 02:30:41.07	12-08 02:31:47.67	✓	✓	✓	✓	✓	✓

*The GNSS-R antenna cable was confirmed in post-processing to not have been plugged in. The USRP data are strictly receiver noise.

∼ Video file exists, but may be corrupted.

https://doi.org/10.5194/egusphere-2026-5057
Preprint. Discussion started: 8 September 2026
© Author(s) 2026. CC BY 4.0 License.

of the subsections below describes the processing of each data stream in more detail. The method is generally similar to that documented in Parvizi et al. (2024).

4.1.1 Lidar and camera

The gray boxes in Fig. 9 are actions that precede this analysis. In the field, we measured the relative positions of the GNSS-R antenna R_0, lidar L_0, each of the i cameras $C_{0,i}$, and I_0, relative to the direct positioning antenna D_0. These are listed in Table 3, in a coordinate system $\hat{t}, \hat{b}, \hat{u}$ corresponding to directions transverse to the GNSS-R antenna boom, along the boom, and up, respectively (see Figs. 5-6). Orientation angles of the cameras were also measured relative to these axes. The relative heading μ_i, measured with respect to $\hat{b}$ and elevation angles ψ_i with respect to the horizontal are given in Table 3 as well.

Each camera's focal length and distortion parameters are estimated using the Matlab camera calibrator app. The fields-of-view are measured in the lab after returning the equipment. These parameters are used to undistort the camera images, which are read directly from the .mp4 files frame by frame.

We use the Matlab lidar toolboxes to read in the point clouds for processing. The files created by the Velodyne lidar are in pcap format. The files created by the Ouster lidar at PGSS are in pcapng format. The Ouster data files are first opened in Wireshark software to convert from pcapng to pcap. Then the converted-to-pcap file and the json file that was output by the lidar are read in using a modified version of the relevant Matlab toolbox function. Each lidar's point cloud is given in a lidar body frame $\hat{x}_L, \hat{y}_L, \hat{z}_L$ specified by the manufacturer, and labeled on Figs. 5-6.

The point clouds provide depth information needed to back project the camera images into three dimensions. The point cloud is cropped to the field-of-view range of the camera, using their position and orientation angles. Then each camera pixel is assigned a depth based on the lidar point cloud, interpolated to the pixel locations. The position of each pixel p relative to the GNSS-R antenna R_0 in 3D space $\boldsymbol{r}^{p/R_0}$ is then back projected using the camera calibration parameters.

To overlay Fresnel zones on the camera images projected to the ground, we begin with the direct antenna position D_0 estimated from the rinex files, and use the relative position $\boldsymbol{r}^{R_0/D_0}$ in Table 3 to estimate the position of the GNSS-R antenna. We compute GPS satellite positions with the day's Yuma almanac from the U.S. Coast Guard (usc), from which we obtain each satellite's position relative to R_0, and its azimuth and elevation angles.

Meanwhile, we crop out points from the lidar point cloud that scattered off the mounting tower and those higher than a cutoff height to remove points from the guy wires and flags, then take the mean $\hat{z}_L$ value of the remaining points to estimate the surface distance below the lidar and thus the GNSS-R antenna h_1. We assume a flat Earth, which is valid for the height of the antenna from the scattering surface.

Given the geometry of the transmitter, receiver, and scattering surface, we compute the parameters x_0, a, b of the specular point horizontal distance from the antenna, and the semi-major and semi-minor axes of the L1 frequency first Fresnel zone ellipse. These define the points $\boldsymbol{r}^{FZ/R_0}$ of the perimeter of the Fresnel zone that are plotted on the camera projections and used to identify the surface areas scattering the GPS signal. From the projection maps, we select satellites of interest, choosing one at high elevation and medium elevation as well as one that is not in the sky.

https://doi.org/10.5194/egusphere-2026-5057
Preprint. Discussion started: 8 September 2026
© Author(s) 2026. CC BY 4.0 License.

We process the GNSS-R data stream to compute SNR for these and show the histograms of the SNR for the first 5 minutes of Part 2 from Pegasus on 8 Dec 2023, anticipating that the strongest reflections will be at this site, having bare ice, and during the period of time in which we know the inline gain to have been manually connected to the USRP.

4.1.2 GNSS REFLECTOMETRY SNR

The original USRP data `.dat` files collected by the USRP contain interleaved int16 in-phase (I) and quadrature (Q) samples recorded at 5 MHz. These files are preprocessed to read the raw I/Q data, convert to real-valued output using a fast Fourier transform, and saved as `.bin` files. The first 5 s of these data files are skipped to eliminate the USRP's automatic gain control settling time. The GNSS-R processing is based on the software-defined receiver (SDR) built in Matlab by Borre et al. (2007). Our SNR calculation builds off the SDR acquisition script. We read the binary data as interleaved sample pairs, separated into in-phase s_I and quadrature s_Q components, and recombined into a complex signal $\tilde{s}_n$ for the GNSS acquisition search. Details on the concepts of coherent and incoherent integration for accumulating the signal power are given in Appendix A.

In short, for a given PRN 1 through 32, the data $\tilde{s}$ are correlated against the known GPS C/A code x, consisting of a repeating sequence of 1000 "chips" unique to a given PRN. The search is performed across multiple possible code phases m and Doppler bins f_D through a Fourier transform. This produces an acquisition map $\hat{S}(m, f_D)$ for each PRN, where stronger values indicate stronger agreement between the recorded signal and the expected satellite code. For each PRN, the maximum value in the acquisition map is identified as the primary peak P_{max} of Eq. (1).

The acquisition method was modified from the original acquisition approach of the open-source SDR of Borre et al. (2007) to use $N_{coh} = 10$, i.e., 10 ms coherent processing blocks.

The data are divided into 10 ms coherent blocks. Sequential blocks over time intervals T_1 and T_2 are grouped into 20 ms pairs. For each pair, the two 10 ms blocks were compared, and the block with the stronger acquisition peak is kept according to Eq. (A10). The weaker block was discarded. This method was used because GPS navigation bit transitions can reduce the strength of a coherent sum if the signal changes sign across the integration period.

Repeating the 10 ms coherent accumulation and taking the larger of every pair of 10 ms blocks, we record the SNR values over time and show a histogram of SNR. These plots are used to check whether some PRNs consistently produced stronger acquisition results than others.

A longer incoherent integration window is also tested to try to improve acquisition as given in Eq. (A9). Multiple retained 10 ms acquisition maps were added together over a longer time window of 100 ms, consisting of the 50 ms of the larger peaks of time intervals T_1 and T_2. The purpose is to check whether persistent signal energy is built up when multiple coherent integration maps were combined.

4.2 GNSS-R RESULTS

Figure 10 shows a map of the surface at the Pegasus site from the lidar and camera projections. The origin is marked with a green 'x' at the reflection antenna R_0. Each camera image is projected onto an approximately trapezoidal area. Only camera pixels spanned by the lidar point cloud are imaged, so although the cameras imaged the horizon and sky, these are not shown

https://doi.org/10.5194/egusphere-2026-5057
Preprint. Discussion started: 8 September 2026
© Author(s) 2026. CC BY 4.0 License.

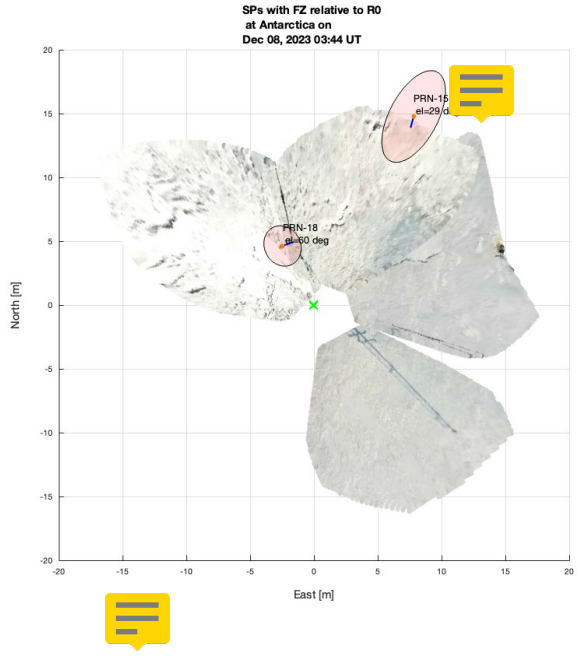


Figure 10. Camera-lidar projected map of surface and select PRN Fresnel zones at Pegasus on 8 Dec 2023 03:44 UT. The green 'x' marks the origin at the 9-m tower.

in the figures because there is no depth information with which to back-project into 3D. Camera 1 to the northwest shows snow shadow ridges and bright sunlit snow. Camera 2 to the north images shadow ridges also, plus some blue ice at about (5, 5) m. Camera 3 images to the east, and the base of the GNSS-IR tower is visible at (14, 4) m. There are color variations in the bare ice as well. Camera 4 to the southeast images the shadow of the 9-m tower. Overplotted on this map are the specular point (orange dot) and Fresnel zones (pink shaded ellipse) for PRNs 18 and 15, with their elevation angles listed. The blue line indicates the direction of motion of the specular point. PRN 18 is at the highest elevation of 60° and its FZ partly encloses a patch of snow. PRN 15 at 29° elevation is less than half imaged by the lidar-projected portion of the camera image.

Figure 11 shows a histogram of the L1 SNR values for the first five minutes of 8 Dec 2023, Part 2, using 10 ms coherent integration for PRN 18 (green) and PRN 15 (red). For reference we also computed the SNR for a satellite known from the GPS almanacs to not be in the sky, PRN 28. All three histograms are fairly similar, which is unexpected since we anticipate a much stronger SNR from PRNs in the sky, relative to the SNR of a PRN not visible. Because there is not a significant difference between the histograms, we then examine the SNR for all GPS satellites.

Figure 12 shows a skyplot of satellites present in the sky at 03:44 UT, at the start of the Pegasus 8 Dec, Part 2, data set. In a sky plot, the horizon is around the perimeter and zenith (90° elevation) at the center. The azimuthal angle from 0° to 360° indicates the direction of the sky that the satellite is in. PRN 18 is at 60° elevation at 330° azimuth, to the north-northwest. For this reason it is anticipated to scatter off the Fresnel zone shown in Fig. 10. Based on this skyplot, we classify satellites as

https://doi.org/10.5194/egusphere-2026-5057
Preprint. Discussion started: 8 September 2026
© Author(s) 2026. CC BY 4.0 License.

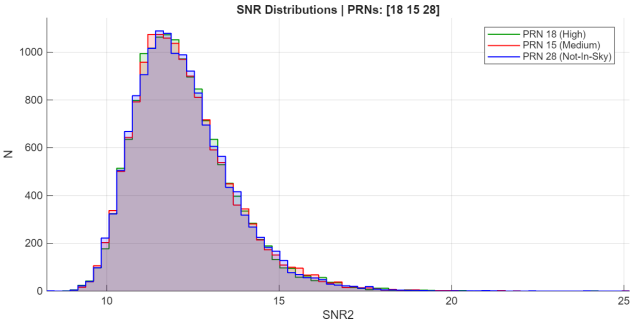


Figure 11. SNR histograms for PRNs 18 (high elevation), 15 (medium), and 28 (not-in-sky) over the five-minute processing run.

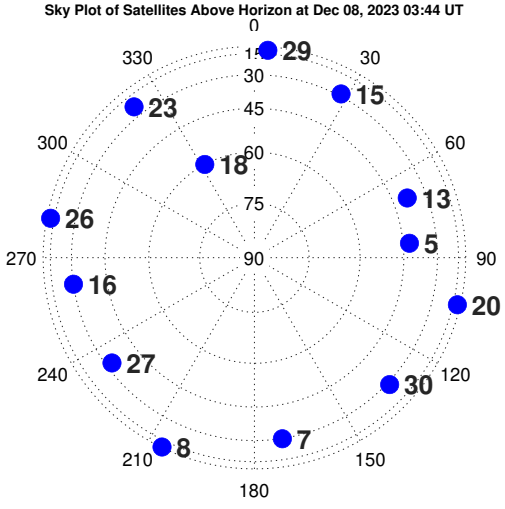


Figure 12. Sky plot of PRNs in view at Pegasus 8 Dec 2023 03:44 UT.

in-sky or out-of-sky PRNs. The in-sky PRN set, reading clockwise in azimuth from 0°, is: [29, 15, 13, 5, 20, 30, 7, 8, 27, 16, 26, 23, 18].

Figure 13 shows histograms of L1 SNR for all 32 GPS satellites, both those that are in the sky (red) and not in the sky (blue). The purple shading results from multiple overlapping blue and red histograms. This comparison is used to check whether PRNs expected to be visible produce different SNR distributions than PRNs that are not expected to be visible. We would expect to see the red (in-sky) distributions differ from the blue, as well as from each other if significant forward-scattered energy from the surface were being collected. We plot the maximum and mean SNR for each PRN on a scatter plot in Fig. 14. There is no significant difference in the mean values for those in the sky versus not. Some in-sky (red) PRNs have higher maximum SNR values in the 5-minute period considered.

Additional filtering could also be considered based on satellite geometry and site conditions. PRNs with azimuths between approximately 180° and 270° can be removed from the expected usable GNSS-R set because this region contained the walking

https://doi.org/10.5194/egusphere-2026-5057
Preprint. Discussion started: 8 September 2026
© Author(s) 2026. CC BY 4.0 License.

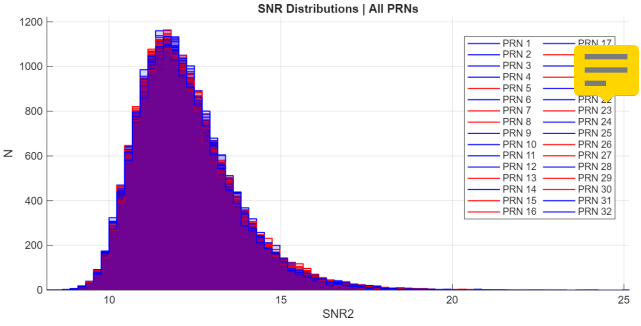


Figure 13. SNR distributions for all 32 PRNs over the five-minute processing run 03:44-03:49 UT on 8 Dec 2023 at Pegasus.

path used for travel to and from the site, had less optimal camera coverage (see Fig. 10), and was more likely to experience strong multipath scattering from the 9-m tower. This would remove PRNs 8, 16, and 27. PRNs 13 and 5 could also be removed because their Fresnel zones are located near the I_0 tower location, making it more likely to be affected by unwanted multipath. However, there is no reason for PRN 30 (with a low maximum SNR) not to be considered, and there is no argument for removing PRN 28, which is not in the sky (and with a high maximum SNR during the period being considered).

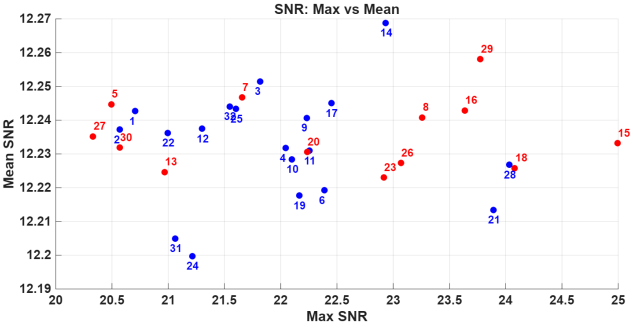
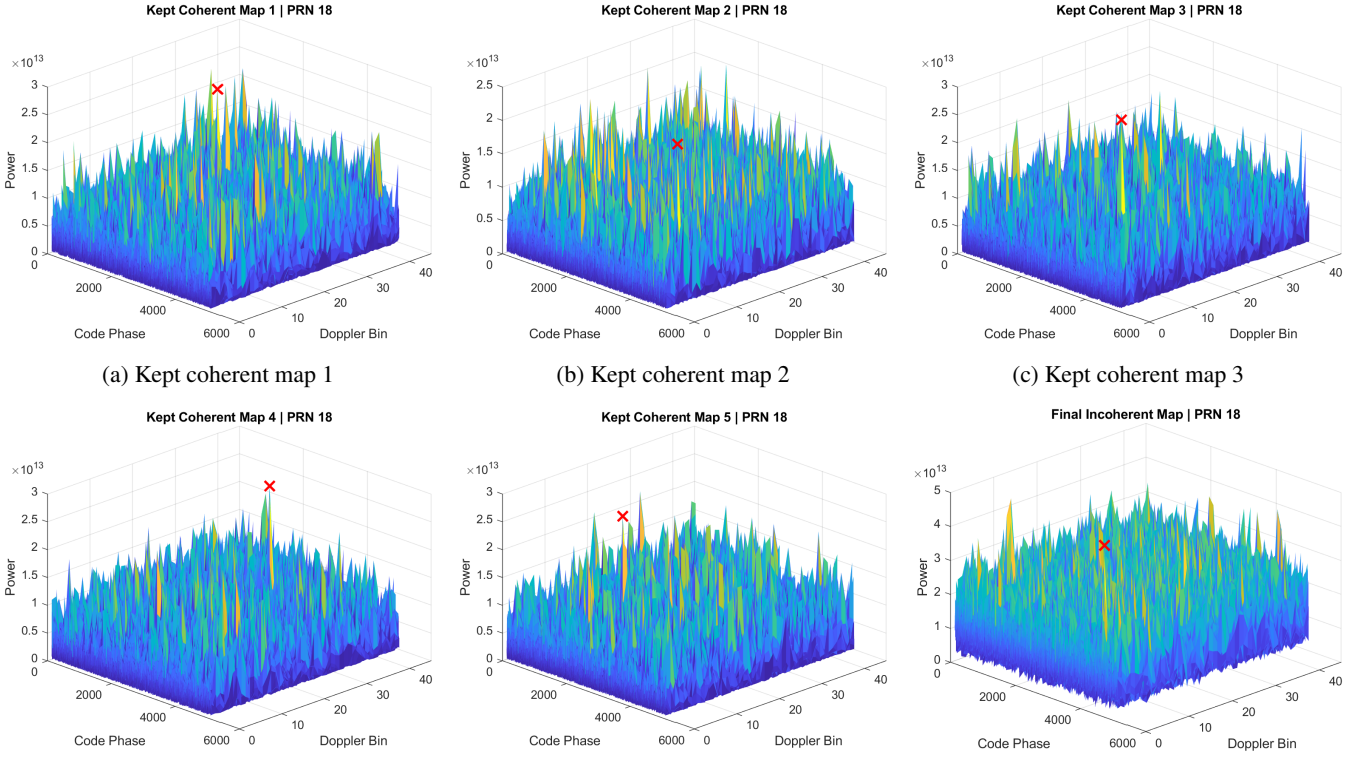


Figure 14. Mean versus maximum SNR for all 32 PRNs. Red labels indicate in-sky PRNs and blue labels indicate out-of-sky PRNs. Red histograms are for satellites in the sky, and blue for those below the horizon.

Even excluding PRNs that might have tower obstructions blocking the signals from reception, the SNR distributions of the remaining PRNs, their SNR means, and SNR maxima also indicate that the satellites whose signals should have cleanly scattered from the surface and those that are not in the sky are not notably different.

To investigate this further, we plot the acquisition search space $\hat{S}(m, f_D)$ for PRN 18 (in the sky). Figure 15 shows (a)-(e) five coherent maps for PRN 18, keeping the larger of T_1, T_2, along with (f) the final incoherently summed map. The peak location changes between the individual coherent maps, and the final incoherent map does not show a clear, stable buildup at one Doppler bin and code phase location. This suggests that the longer incoherent summation mainly increases the background level rather than strengthening a persistent reflected GNSS signal. As a result, incoherent sums of the data result in noise accumulation rather than a clear strengthening of a stable GNSS reflection.

https://doi.org/10.5194/egusphere-2026-5057
Preprint. Discussion started: 8 September 2026
© Author(s) 2026. CC BY 4.0 License.



(a) Kept coherent map 1 (b) Kept coherent map 2 (c) Kept coherent map 3

(d) Kept coherent map 4 (e) Kept coherent map 5 (f) Final incoherent map

Figure 15. (a)-(e) Acquisition maps for 10 ms coherent integration and (f) final incoherent sum for PRN 18. The red marker indicates the strongest peak in each map.

5 GNSS INTERFEROMETRIC REFLECTOMETRY

5.1 GNSS-IR METHOD

The processing workflow for the GNSS-IR data is shown in Fig. 16. The overall approach for the lidar and cameras are the same as for the GNSS-R analysis. The main exception is that satellite and Fresnel zone positions are computed relative to the IR antenna I_0. While the GNSS-IR method is not strictly a snapshot of a single location, but uses the entire swath of ground scanned by the Fresnel zone over an entire rising or setting interval, the example camera images give a sense of the surface at which a PRN's signal scatters for a part of the satellite's data segment used.

Observation files in RINEX 3 format were downloaded from the Trimble geodetic antenna and receiver systems spanning 20 November to 9 December 2023 of the experiment for the 2-m towers at each site. The downloaded files were organized into a local directory following the required naming convention of the gnssrefl toolkit Larson (Accessed 03 September 2024). Docker was then used to access the open-source GNSS reflectometry Python tools and libraries, with the `gnssrefl` package cloned from its repository for local processing.

https://doi.org/10.5194/egusphere-2026-5057
Preprint. Discussion started: 8 September 2026
© Author(s) 2026. CC BY 4.0 License.

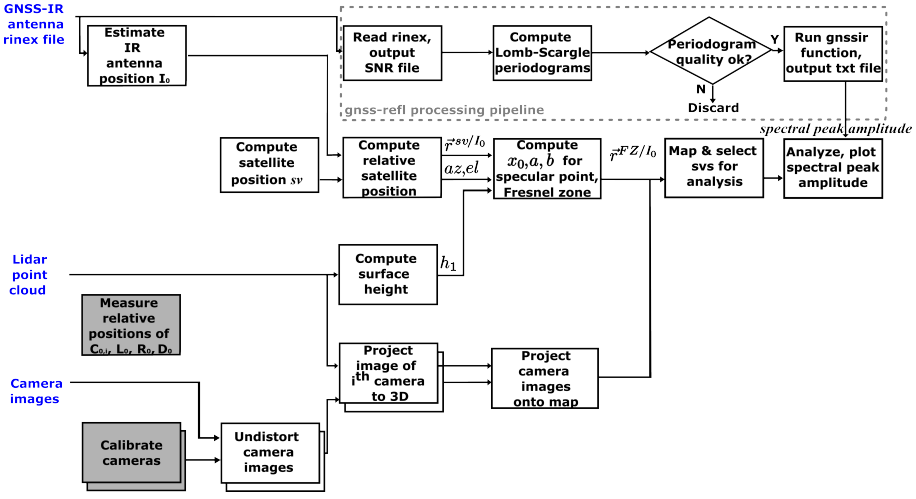


Figure 16. GNSS-IR post-processing workflow. Blue text identifies data files. Gray boxes identify calibration steps that are done offline.

The GNSS-IR processing (gray dashed box in Fig. 16) is performed using the open source gnssrefl tools available on Github (Larson, 2024, Accessed 03 September 2024). This is a set of python tools that can be built and run with a Docker container (Larson, Accessed: 03 September 2024).

Given a Rinex 3 file over a 24-hour period containing SNR outputs and 0° mask angle, the SNR data at multiple frequencies are extracted from satellites at elevation angles below 30°. These SNR files were used to generate two types of diagnostic plots: periodogram plots organized by azimuthal quadrants around the receiver, and plots showing reflection height H_R from Eq. (2), spectral peak amplitude (SPA), and peak-to-noise ratio.

Also provided is an estimate of the peak-to-noise ratio of the Lomb-Scargle periodogram, where the noise is defined as the mean value of the amplitude of the periodogram over the whole interval between user-selected reflector heights H_R, corresponding to wavelength as seen in Eq. (2) (Larson, Accessed: 03 September 2024). The spectral peak amplitude is the maximum value of the spectrum. There are two quality control checks: the peak-to-noise ratio is filtered to be at least 4, which is considered to be high quality signal for polar surfaces (Larson, Accessed: 03 September 2024); and the reflection height filter is set to include heights greater than 1 meter to remove outliers. Both filters are applied in Matlab post-processing. The parameters for data selection can be adjusted to output files of the SNR for individual PRNs whose estimates of H_R, peak-to-noise ratio and spectral peak amplitude can be plotted. In this work we focus on the spectral peak amplitude from GPS satellites (not GloNASS).

5.2 GNSS-IR RESULTS

Figure 17 shows a top-down view of the surface relative to the IR tower as imaged by the cameras at (a) Pegasus on 8 Dec 2023, 03:44 UT (similar to Fig. 10), and (b) at Phoenix on 27 Nov 2023 at 04:11 UT. The origin is at the 2-m tower I_0, marked

https://doi.org/10.5194/egusphere-2026-5057
Preprint. Discussion started: 8 September 2026
© Author(s) 2026. CC BY 4.0 License.

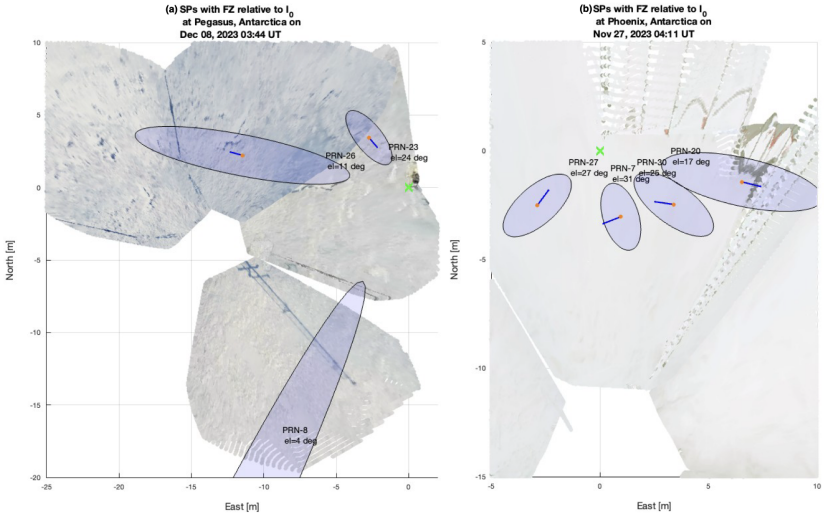


Figure 17. Camera projections and L1 frequency first Fresnel zones from (a) PGSS-IR and (b) PHNX-IR. The green 'x' marks the origin at the 2-m tower.

with the green 'x'. The camera images are projected about the 9-m tower at which they were mounted, so the 9-m tower is not visible, but the camera images do map the surface between and to the 2-m tower.

Pegasus has a heterogeneous surface of snow-covered and bare ice, visible from the snow ridge shadows and blue tinge, respectively. Phoenix is a snow-covered surface. The camera images have been color balanced across all four cameras, by normalizing each of the red, green, and blue histograms between cameras. This makes the white of the snow appears as the same shade across all camera images independent of illumination variations. The green 'x' is near the base of the 2-m tower. At Phoenix the camera projection of the pixels to the north of the origin become striped because the pixels are being mapped to lidar scan locations. The red of the flags marking the experiment area are visible to the east-northeast of the origin, with the shadows and poles projected north and outward, again because they are mapped to lidar points. The solar array obstructs the projection of camera pixels, creating an invisible region northward of (7, 0) m. The surface is snow covered with snow shadow variations in the surface barely visible due to lower contrast in the illumination on this day, but separately from that, the surface is overall more homogeneously snowy than at Pegasus.

At Pegasus the area well-imaged near the IR tower (PG02) is to its west. At Phoenix the camera-imaged area is to the south of the IR tower. Overplotted on each of these plots are Fresnel zones ellipses, shaded blue for satellites whose signals are reflecting off the surface and received at PG02 and PHNX, respectively, at the time the image is taken. Blue line segments show the direction the FZs are moving at this time.

Because the IR tower is shorter at each site, the FZs are closer to the tower even at low elevations. The GNSS-IR technique for computing reflection height and spectral peak amplitude requires an elevation scan, which we restrict to be from 5-25°, to produce one SPA estimate. So, unlike GNSS-R, there is no SPA measurement that will correspond to these individual FZ

https://doi.org/10.5194/egusphere-2026-5057
Preprint. Discussion started: 8 September 2026
© Author(s) 2026. CC BY 4.0 License.

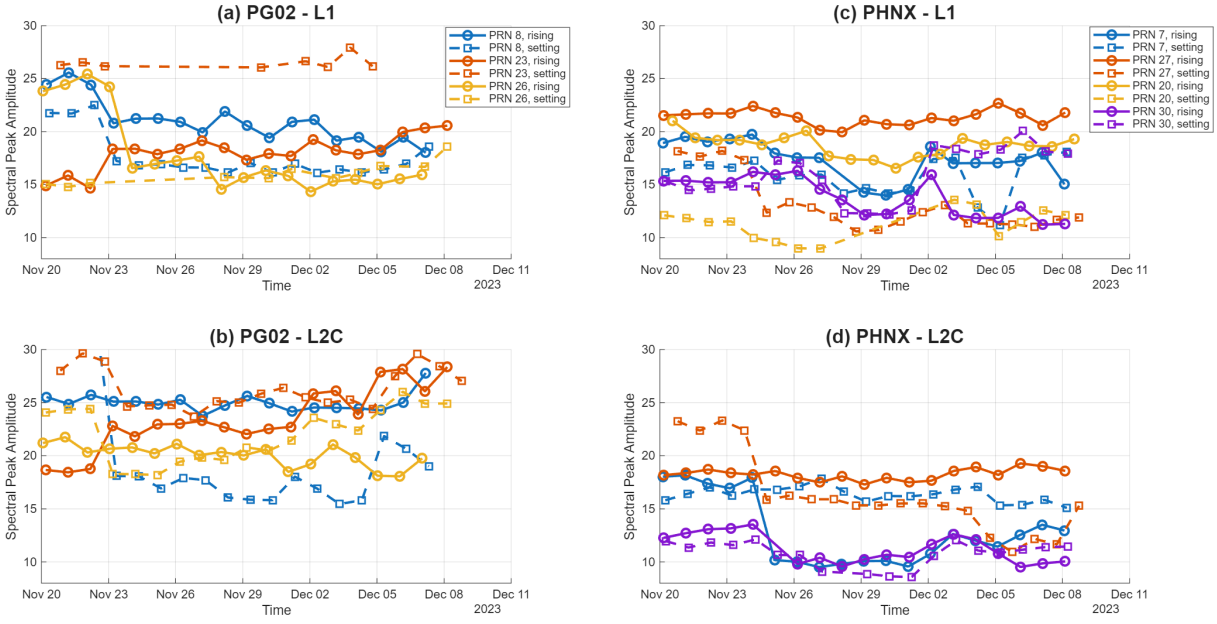


Figure 18. Spectral Peak Amplitude in units of V/V versus time for the selected PRNs, DOY 324-342

ellipses. However, these ellipses and their direction of motion indicate part of the sampled surface area that is included in the GNSS-IR elevation scan.

At Pegasus (PG02), PRN 23 is at 24° elevation and the direction of movement shows it to be rising, and PRN 26 is at 11° and setting. The PRN 8 FZ is to the south and only partly imaged by the cameras. At Phoenix (PHNX), PRN 30 is at 25° and rising, and PRN 20 is at 17° and setting. PRNs 7 and 27 at this moment are above 25°, so their data are not used at this moment. However, their data prior to rising above 25° and after setting below 25° at other times of the day, are processed.

Figure 18 shows the SPA estimated over time from the PRNs whose Fresnel zones were shown in the camera images of Fig 17 at (a) Pegasus (PG02) L1 frequency, (b) Phoenix (PHNX) L1, (c) PG02 at L2C frequency, and (d) PHNX L2C. The SPA curves are selected for the azimuth range in the viewing area of the camera, i.e., 90-270° for PG02 (to the west), and 180-360° for PHNX. Rising and setting intervals are separated for a given satellite since they produce separate estimates and scan different areas of the surface. There is no L2C data for PRN 20, which in 2023 was a Block IIR satellite vehicle number (SVN) 51, pre-dating the satellites that broadcast L2C.

At PG02 (Figs. 18(a) and (c)) several of the curves drop by an SPA of 5-10 from November 22-23. This marks the point at which we lowered the PG02 antenna on-site. Lowering the antenna has a discernible effect not only on reflection height (not shown), but also by reducing the estimated SPA. At PHNX, shown in Figs. 18(b) and (d), there was no manual movement of the antenna. However, in the L2C data, the SPA estimate drops between Nov 24th and 25th for PRN 27 setting and PRN 7 rising, by about 8 units. Based on the FZ movement shown in Fig. 10(b), this corresponds to an area southeast of the PHNX tower, which would have been undisturbed by airfield activities or fieldwork access. While this could correspond to environmental

https://doi.org/10.5194/egusphere-2026-5057
Preprint. Discussion started: 8 September 2026
© Author(s) 2026. CC BY 4.0 License.

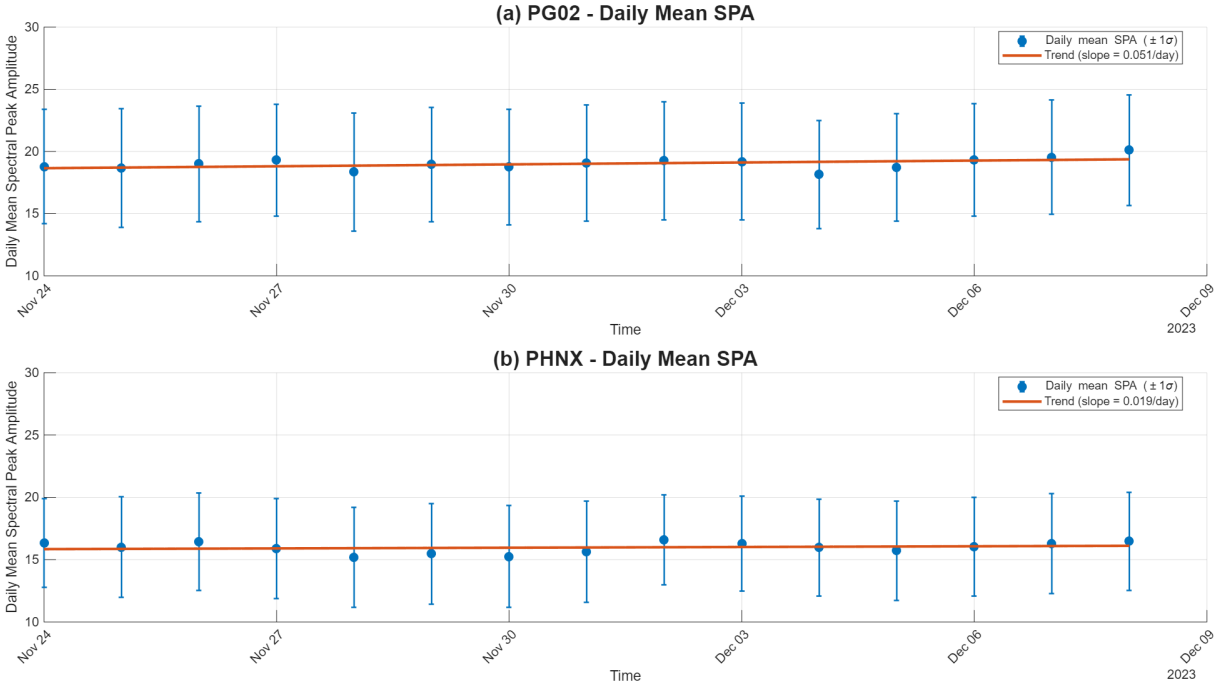


Figure 19. Daily Mean SPA (Volts/Volt) vs. time, L2C Frequency, All PRNs

conditions, we would expect a similar trend from those PRNs at L1. There is a drop of 2 units in the L1 PRN 7 rising SPA, and a 5 unit drop in the L1 PRN 27 setting SPA. This may indicate that a SPA variation in the environment is more readily observed in the L2C frequency. On the other hand, PHNX L1 and L2C do not show similar trends for PRN 7, setting, in the 2-6 December interval. The satellite geometry would put this scan to the southwest of PHNX, which is where the surface is groomed for airfield operations. So this may be a result of artificial conditions and human activity.

Figure 19 shows the daily mean and standard deviation of the L2C-derived spectral peak amplitude values collected over the course of the experiment, excluding the dates prior to the PG02 relocation. The average spectral peak amplitude for each day uses the selected azimuth region for each corresponding site, similar to Figure 18, but uses all available PRNs that scan those regions (south of PHNX, west of PG02) from 24 November to 8 December.

In Fig. 19(a), at PG02, there is an increasing trend in the SPA estimates overall, of about 0.05 units per day. At PHNX there is a rate of increase in SPA that is smaller, at 0.019 units per day. The daily standard deviation of PG02 is about 5, but about 3 at PHNX.

Aggregating the data at each site over time, Figure 20 shows histograms of the SPA values for each site over the course of the experiment from 23 November through 8 December, after all antenna relocations are complete. The histogram for each site used the selected observable azimuth region, all available PRNs, and L2C frequency. Along with the histogram is the indcation of the mean value for each site as well as the 1 sigma standard deviation over all time. The histogram at PG02 has a higher mean and larger standard deviation than the one at PHNX.

https://doi.org/10.5194/egusphere-2026-5057
Preprint. Discussion started: 8 September 2026
© Author(s) 2026. CC BY 4.0 License.

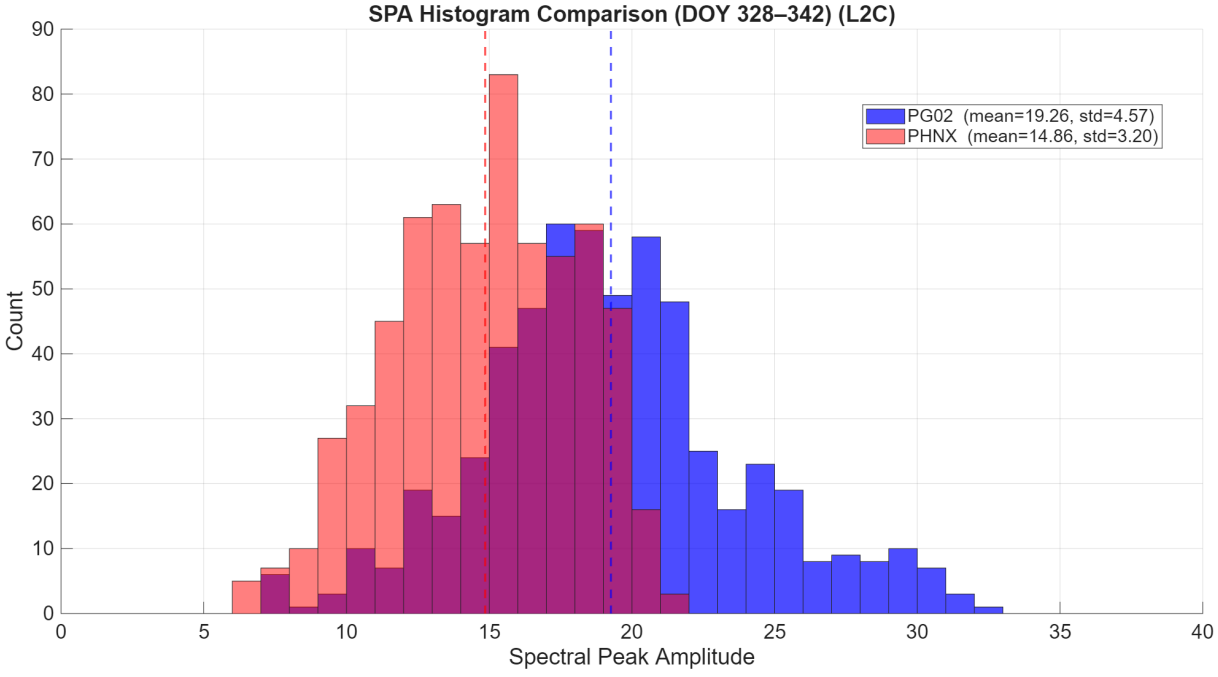


Figure 20. Spectral Peak Amplitude (Volts/Volt) Histogram, Site Comparison

While it is tempting to attribute this difference in SPA of the histograms to the differences of the surface between each site, there is one factor we were unable to control for: the different antenna-receiver pairs at each site. The pre-existing site PHNX has Septentrio equipment, whereas PG02 uses Trimble NetR9. We attempted to control for equipment differences by processing the PG10 and PX10 positioning data which had identical Trimble equipment, but because the 9-m towers were set up primarily to be used for positioning, they did not have SNR data. For this reason, while Fig. 20 clearly indicates a difference in SPA response between the two ice shelf sites, how much of that is environmental and how much might be due to internal antenna and receiver-specific gain settings, multipath-limiting algorithms, or other factors that might affect the periodograms, cannot be determined.

6 Conclusions

We conducted fieldwork in Antarctica in November and December 2023 to test GNSS reflectometry in multiple modalities as a method for sensing surface conditions on an ice shelf. This is the first combined GNSS-R and GNSS-IR reflectometry data collected with shared fields-of-view from the Antarctic ice shelf, and to our knowledge the first time GNSS-R data have been collected from a glaciated surface. The antennas were mounted on two static towers, 2 m and 9 m high respectively, at each of two contrasting sites, in terms of surface conditions, Pegasus and Phoenix airfield. Accompanying positioning antenna, lidar and camera maps of the ice shelf field of view were also obtained.

https://doi.org/10.5194/egusphere-2026-5057
Preprint. Discussion started: 8 September 2026
© Author(s) 2026. CC BY 4.0 License.

Both the GNSS-R and the GNSS-IR experiments were inconclusive. The GNSS-R SNR processing showed that reflected signals did not appear to have been acquired, demonstrated here with data from Pegasus. Some PRNs produced stronger maximum SNR values and occasional high SNR maxima, especially among the in-sky PRNs. However, the SNR distributions for all 32 PRNs overlapped significantly. There was no distinct separation between in-sky and out-of-sky PRNs.

For GNSS-R, using sequences of 10 ms coherent integration, the strongest peak did not remain in one consistent Doppler bin or code phase location. Instead, the peak moves between acquisition maps. As a result, longer incoherent integration did not produce a clear buildup of reflected signal energy. Based on these results, we find that for GNSS-R, SNR processing should be treated as a signal acquisition and quality-screening step before using the data for surface-condition analysis.

The analysis of GNSS-IR yielded numerous spectral peak amplitude estimates that were of sufficient quality at each site. There were a slight increasing trend in the mean SPA at Pegasus, and a minimal decreasing trend over time at Phoenix. Comparing SPA estimates between sites, there were clear differences in the mean and standard deviation of the histograms. The mean SPA for the partially bare ice site was 4 units larger than for the snow-covered site, and with a larger standard deviation. However, any possible contribution to this difference due to the differing equipment sited cannot be distinguished here.

Future analysis of the data should consider advanced signal processing techniques that to increase the SNR from the GNSS-R data sets. For GNSS-R field experiments, additional inline gain may be required. Mounting the GNSS-R antenna closer to the surface may help capture more scattered energy, as in (Parvizi et al., 2024); however, this reduces the field of view of the GNSS-R sensing zone. The inability to sense larger area swaths of the surface would reduce the utility, if its efficacy can be shown, of a ground-based GNSS-R remote sensing method. For future GNSS-IR experiments, comparison of different ice shelf sites with identical equipage will help control for a possible confounding factor in the differences between sites observed in this work.

Data availability. The GNSS-R, lidar, and camera data are available at https://www.unavco.org/data/doi/10.7283/61M5-8Z10. The PHNX data are available at https://doi.org/10.7283/47RJ-XE12.

Appendix A: Background on GPS signal acquisition via coherent and incoherent integration

The process by which a receiver determines whether a GPS satellite signal exists in the incoming data from the antenna is called GPS signal acquisition. In short, the incoming signal is downconverted and de-spread to concentrate the signal above the noise level by being correlated with a replica of one satellite's known pseudorandom noise (PRN) coarse acquisition (C/A) code sequence x. Each satellite is assigned its own unique PRN code (Misra and Enge, 2006).

To attempt to acquire satellites, the front end of a receiver first downsamples the signal to an intermediate frequency f_{IF} and digitizes it to give:

https://doi.org/10.5194/egusphere-2026-5057
Preprint. Discussion started: 8 September 2026
© Author(s) 2026. CC BY 4.0 License.

$$s_{IF}(nT_s) = P_s D(nT_s - m'T_s)x(nT_s - m'T_s)$$
$$\cos\left(2\pi(f_{IF} + f'_D)nT_s + \theta\right) + w_{IF}(nT_s) \tag{A1}$$

where n is the sample number, $T_s = f_s^{-1}$ is the sampling period corresponding to sampling frequency f_s, P_s is the digitized received power, D is the unknown navigation data bit, $m'T_s$ is the unknown code delay, x is the C/A code for one satellite, f'_D is the unknown Doppler frequency shift due to the relative motion between the satellite and the receiver, θ is the unknown phase offset, and w_{IF} is multipath and thermal noise.

Each PRN code is made of 1023 rectangular pulse "chips" of duration T_c, and the full sequence of chips repeats every $T_{C/A} = 1$ ms. The navigation data D is also a sequence of rectangular pulses transmitted at 50 bits per second with 20 ms of bit duration. The navigation data contains the satellite health status, ephemerides for computing satellite position and velocity, clock bias and ionospheric correction parameters, and satellite almanac information (Misra and Enge, 2006) (Tsui, 2005).

In a receiver, correlation of s_{IF} with a replica of x for different time shifts m and Doppler f_D yields a matrix $\hat{S}(m, f_D)$ of correlation power as a function of code delay and frequency space, where $\hat{m}, \hat{f}_D$ are the delay and Doppler frequency at which the correlation peak occurs.

The most basic form of signal acquisition is via coherent integration. Because the phase θ is unknown, the downconverted digitized signal s_{IF} is multiplied with a locally generated cosine to create in-phase samples s_I, and separately multiplied by a sinusoid for quadrature-phase samples s_Q, at a given Doppler f_D.

$$s_{I,n} = s_{IF}(nT_s)\cos\left(2\pi\left(f_{IF} + f_D\right)nT_s\right) \tag{A2}$$
$$s_{Q,n} = s_{IF}(nT_s)\sin\left(2\pi\left(f_{IF} + f_D\right)nT_s\right) \tag{A3}$$

or, in complex form,

$$\tilde{s}_n = s_{IF}(nT_s)\exp(2\pi j(f_{IF} + f_D)nT_s) \tag{A4}$$

where the tilde denotes a complex value.

Each $s_{I,n}$ and $s_{Q,n}$ is correlated with a receiver-generated replica PRN code x for the coherent integration time T_{coh}, which is an integer number N_{coh} of repetitions of the full PRN code duration $T_{C/A}$.

$$T_{coh} \equiv N_{coh}T_{C/A} \tag{A5}$$

Correlation over T_{coh} is carried out by first computing the correlation for each code repetition of duration $T_{C/A}$ consisting of N samples and then summing the correlations over N_{coh} segments.

$$T_{C/A} = NT_s \tag{A6}$$
$$\tilde{S}_k(m, f_D) = \frac{1}{N}\sum_{n=1}^{N}\tilde{s}_n x((n-m)T_s) \tag{A7}$$

https://doi.org/10.5194/egusphere-2026-5057
Preprint. Discussion started: 8 September 2026
© Author(s) 2026. CC BY 4.0 License.

Each summation index (e.g., n) will be associated with one specific summation (e.g., sum over one C/A code repetition), to avoid ambiguity.

The N_{coh} correlation outputs are then summed to compute autocorrelation power $\bar{\tilde{S}}$:

$$\bar{\tilde{S}}(m, f_D) \quad = \quad \sum_{k=1}^{N_{coh}} \tilde{S}_k(m, f_D) \tag{A8}$$

where the overbar indicates summation. Here the index k counts over each code repetition. To estimate the Doppler frequency $\hat{f}_D$, the correlation process given by Eq. (A7) may be iterated for frequencies within a band around the intermediate frequency f_{IF}.

Assuming the phase θ is constant over the integration time, coherent integration over longer time segments $N_{coh} > 1$ can increase the signal power, enabling acquisition, as long as the unknown data bit D in s_{IF} does not change sign within time T_{coh}. However, due to the possibility of a navigation data bit transition (yielding a $180°$ phase shift), coherent integration is often restricted to a few milliseconds (Misra and Enge, 2006) (Tsui, 2005).

Another way to compensate for the unknown phase θ and for possible data bit transitions is to use the power from the quadrature-phase accumulation as well as the in-phase by the taking the magnitude of the complex correlation power for the ith segment of duration T_{coh}:

$$S_{inc} \quad = \quad \sum_{i=1}^{N_{inc}} (|\bar{\tilde{S}}_i(m, f_D)|^2) \tag{A9}$$

With incoherent integration over a number $N_{inc} > 1$ of segments, each of which is coherently accumulated, the square magnitude $|\bar{\tilde{S}}|^2$ of the correlation power is accumulated. Incoherent integration permits a longer integration time, but the absolute value and squaring operations also increase the noise.

For $N_{inc} = 1$, Eq. (A9) represents incoherent detection of a coherently integrated signal. To compensate for the possibility of a data bit flip within the data segment coherently integrated, comparison of the correlation peaks of two consecutive data segments helps determine the data segment in which a data bit flip has not occurred, such that it may be used for acquisition.

Given a data time series from time $t = [t_0, t_0 + T_d]$ of duration $T_d = 2T_{coh}$, the data are divided into two equal duration segments of time $T_1 = [t_0, t_0 + T_d/2]$ and $T_2 = [t_0 + T_d/2, t_0 + T_d]$. The correlation power $\hat{S}$ used for the acquisition metric for $N_{inc} = 1$ may then be chosen as:

$$\hat{S} = \begin{cases} |\bar{\tilde{S}}_{T_1}|^2, & \max_m(|\bar{\tilde{S}}_{T_1}|^2) > \max_m(|\bar{\tilde{S}}_{T_2}|^2) \\ |\bar{\tilde{S}}_{T_2}|^2, & \text{else} \end{cases} \tag{A10}$$

where the maximum is taken over all time shifts m at each Doppler.

Author contributions. SD is lead PI and coordinated the overall effort including experiment design, fieldwork, analysis and writing. AFB is the co-PI and supported experiment design, led the conduct of fieldwork, and edited the manuscript. JW completed the final form of

https://doi.org/10.5194/egusphere-2026-5057
Preprint. Discussion started: 8 September 2026
© Author(s) 2026. CC BY 4.0 License.

GNSS-R analysis and wrote the GNSS-R method results. AW completed the GNSS-IR analysis and wrote the GNSS-IR method and results. RP developed the earlier version of GNSS-R processing, the data collection scripts, and wrote the appendix. CA designed and fabricated the hardware mounting and generated the CAD diagrams of the field sites. AV contributed the analysis of histograms. HK contributed GNSS-R analysis to establish when the USRP was unplugged from the antenna. LG produced the camera calibrations. KL advised on the use of the GNSS-IR processing methods.

Competing interests. No competing interests are present

Acknowledgements. The PHNX receiver and antenna information came from the manufacturer websites https://www.septentrio.com/en/products/gnss-receivers/gnss-reference-receivers/polarx-5 and https://www.navtechgps.com/septentrio_polant_x_mf_high_performance_multi_frequency_antenna_/ accessed 27 May 2026. We acknowledge: our collaborator Doug MacAyeal; former students who worked directly on the effort Arthur Baverel, Clara Martin Munio Zulaica, Seth Graham; Shahrukh Khan, Li Pan, Lan Tran; Students of the Space Weather Lab, NavLab, and Robotics Lab for hardware and software assistance; Illinois Institute of Technology Department Staff for shipping fieldwork assistance; Neel Pandeya of Ettus for technical support optimizing the USRPs for Antarctic data collection; fieldwork support of Mike Jackson of NSF; Randy Jones, Troy Juniel, Crary Lab staff, Gabe Menkhus and the riggers, Berg Field Center and Mechanical Equipment Center, Antarctic Services Contractors; Mark Seefeldt and Erika Schrieber and Joe Pettit of EarthScope for the PHNX station data and assistance processing rinex files from PG02, PG10, and PX10.

This effort was supported by the National Science Foundation Awards 1940473 and 1940483, and the NASA Illinois Space Grant Consortium. Geospatial support for this work provided by the Polar Geospatial Center under NSF-OPP awards 1043681, 1559691, 2129685, and 2434541.

https://doi.org/10.5194/egusphere-2026-5057
Preprint. Discussion started: 8 September 2026
© Author(s) 2026. CC BY 4.0 License.

References

GPS NANUS, ALMANACS, OPS ADVISORIES, & SOF, US. Department of Homeland Security, https://www.navcen.uscg.gov/?pageName=gpsAlmanacs, https://www.navcen.uscg.gov/?pageName=gpsAlmanacs.

Banwell, A., Willis, I., Macdonald, G., and et al.: Direct measurements of ice-shelf flexure caused by surface meltwater ponding and drainage, Nat Commun, 10, 730, https://doi.org/10.1038/s41467-019-08522-5, 2019.

Banwell, A. F., MacAyeal, D. R., and Sergienko, O. V.: Breakup of the Larsen B Ice Shelf triggered by chain reaction drainage of supraglacial lakes, Geophysical Research Letters, 40, 5872–5876, https://doi.org/https://doi.org/10.1002/2013GL057694, 2013.

Banwell, A. F., Willis, I. C., Stevens, L. A., Dell, R. L., and MacAyeal, D. R.: Observed meltwater-induced flexure and fracture at a doline on George VI Ice Shelf, Antarctica, Journal of Glaciology, p. 1–14, https://doi.org/10.1017/jog.2024.31, 2024.

Borre, K., Akos, D. M., Bertelsen, N., Rinder, P., and Jensen, S. H.: A software-defined GPS and Galileo receiver: a single-frequency approach, Springer Science & Business Media, 2007.

Chew, C., Reager, J. T., and Small, E.: CYGNSS data map flood inundation during the 2017 Atlantic hurricane season, "scientific reports", 8, 2018.

Datta-Barua, S., Parvizi, R., Khan, S., Baverel, A., Johnson, R., and Banwell, A. F.: Lake Ice Surface Type Correlation With GNSS Surface Reflectivity, IEEE Transactions on Geoscience and Remote Sensing, 63, 1–10, https://doi.org/10.1109/TGRS.2025.3603893, 2025.

Fricker, H. A., Galton-Fenzi, B. K., Walker, C. C., Freer, B. I. D., Padman, L., and DeConto, R.: Antarctica in 2025: Drivers of deep uncertainty in projected ice loss, Science, 387, 601–609, https://doi.org/10.1126/science.adt9619, 2025.

Fürst, J. J., Durand, G., Gillet-Chaulet, F., Tavard, L., Rankl, M., Braun, M., and Gagliardini, O.: The safety band of Antarctic ice shelves, Nature Climate Change, 6, 479–482, https://doi.org/10.1038/nclimate2912, 2016.

Hanna, E., Pattyn, F., Navarro, F., Favier, V., Goelzer, H., van den Broeke, M. R., Vizcaino, M., Whitehouse, P. L., Ritz, C., Bulthuis, K., and Smith, B.: Mass balance of the ice sheets and glaciers ‚Äì Progress since AR5 and challenges, Earth-Science Reviews, 201, 102 976, https://doi.org/https://doi.org/10.1016/j.earscirev.2019.102976, 2020.

Larson, K. M.: Unanticipated Uses of the Global Positioning System, Annual Rev. Earth and Planet. Sci., 47, 19–40, https://doi.org/10.1146/annurev-earth-053018-060203, 2019.

Larson, K. M.: gnssrefl: an open source python software package for environmental GNSS interferometric reflectometry applications, GPS Solutions, 28, 165, https://doi.org/10.1007/s10291-024-01694-8, 2024.

Larson, K. M.: gnssrefl v3.6.8, https://github.com/kristinemlarson/gnssrefl, Accessed 03 September 2024.

Larson, K. M.: Understanding - gnssrefl documentation, available at https://gnssrefl.readthedocs.io/en/latest/pages/understand.html, Accessed: 03 September 2024.

Larson, K. M., Wahr, J., and Munneke, P. K.: Constraints on snow accumulation and firn density in Greenland using GPS receivers, Journal of Glaciology, 61, 101–114, https://doi.org/10.3189/2015JoG14J130, 2015.

Misra, P. and Enge, P.: Global positioning system: Signals, measurements and performance second edition, 2006.

Parvizi, R., Khan, S., Datta-Barua, S., and Banwell, A. F.: Surface Reflectivity Variations of global navigation satellite signals from a Mixed Ice and Water Surface, NAVIGATION, 71, 1, https://doi.org/doi:10.33012/navi.614, 2024.

Scambos, T., Hulbe, C., and Fahnestock, M.: Climate-induced ice shelf disintegration in the Antarctic Peninsula, Antarctic Research Series, 79, https://doi.org/10.1029/AR079p0079, 2003.

https://doi.org/10.5194/egusphere-2026-5057
Preprint. Discussion started: 8 September 2026
© Author(s) 2026. CC BY 4.0 License.



Scambos, T., Fricker, H. A., Liu, C.-C., Bohlander, J., Fastook, J., Sargent, A., Massom, R., and Wu, A.-M.: Ice shelf disintegration by plate bending and hydro-fracture: Satellite observations and model results of the 2008 Wilkins ice shelf break-ups, Earth and Planetary Science Letters, 280, 51–60, https://doi.org/https://doi.org/10.1016/j.epsl.2008.12.027, 2009.

Shean, D. E., Christianson, K., Larson, K. M., Ligtenberg, S. R., Joughin, I. R., Smith, B. E., Stevens, C. M., Bushuk, M., and Holland, D. M.: GPS-derived estimates of surface mass balance and ocean-induced basal melt for Pine Island Glacier ice shelf, Antarctica, The Cryosphere, 11, 2017.

Siegfried, M., Medley, B., Larson, K., Fricker, H., and Tulaczyk, S.: Snow accumulation variability on a West Antarctic ice stream observed with GPS reflectometry, 2007–2017, Geophysical Research Letters, 44, 7808–7816, 2017.

Survey, C. G.: PPP - Precise Point Positioning, Retrieved July 23, 2026.

Tsui, J. B.-Y.: Fundamentals of global positioning system receivers: a software approach, vol. 173, John Wiley & Sons, 2005.

https://doi.org/10.5194/egusphere-2026-5057
Preprint. Discussion started: 8 September 2026
© Author(s) 2026. CC BY 4.0 License.

Table 2. DATA COLLECTION TIMES AT PGSS IN 2023

Local Date mm-dd	Part	Duration min	UT Start Time mm-dd HH:MM:SS	UT End Time mm-dd HH:MM:SS	USRP	lidar	Cam 1	Cam 2	Cam 3	Cam 4
11-23*	1	1	11-23 01:58:41.90	11-23 01:59:48.62	✓	✓	✓	✓	✓	✓
	2	1	11-23 03:57:25.74	11-23 03:58:32.31	✓	✓	✓	✓	✓	✓
	3	60	11-23 04:01:50.87	11-23 05:01:56.89	✓	✓	✓	✓	✓	✓
11-27	1	1	11-26 22:07:32.52	11-26 22:08:39.12	✓	✓	✓	✓	✓	✓
	2	60	11-26 22:09:38.03	11-26 23:09:43.77	✓	✓	✓	✓	✓	✓
	3	60	11-26 23:11:50.86	11-27 00:11:56.58	✓	✓	✓	✓	✓	✓
	4	60	11-27 00:12:51.33	11-27 01:12:57.26	✓	✓	✓	✓	✓	✓
11-28	1	1	11-27 21:55:49.62	11-27 21:56:56.25	✓	✓	✓	✓	✓	✓
	2	60	11-27 21:58:06.21	11-27 22:58:12.14	✓	✓	✓	✓	✓	✓
	3	60	11-27 23:07:35.77	11-28 00:07:41.62	✓	✓	✓	✓	✓	✓
	4	60	11-28 00:12:26.49	11-28 01:12:32.35	✓	✓	✓	✓	✓	✓
12-01	1	1	11-30 21:56:37.60	11-30 21:57:44.22	✓	✓	✓	✓	✓	✓
	2	60	11-30 21:59:45.26	11-30 22:12:06.41	✓	✓	✓	~	~	~
	3	n/a	No text file available.		✓	✓	✓	~	~	~
	4	30	11-30 23:33:20.58	12-01 00:03:26.97	✓	✓	✓	✓	✓	✓
	5	60	12-01 00:09:03.52	12-01 01:09:09.47	✓	✓	✓	✓	✓	✓
12-05	1	0	12-04 22:07:06.70	12-04 22:07:13.50		✓	~	~	~	~
	2	1	12-04 22:10:15.86	12-04 22:11:22.48	✓	✓	✓	✓	✓	✓
	3	60	12-04 22:13:51.25	12-04 23:13:57.38	✓	✓	✓	✓	✓	✓
	4	60	12-04 23:19:30.08	12-05 00:19:36.05	✓	✓	✓	✓	✓	✓
	5	60	12-05 00:21:47.47	12-05 01:21:53.54	✓	✓	✓	✓	✓	✓
12-07	1	1	12-07 03:29:44.37	12-07 03:30:50.95	✓	✓	✓	✓	✓	✓
	2	n/a	No text file available.		✓	✓	✓	~	~	~
	3	1	12-07 04:33:39.87	12-07 04:34:46.49	✓	✓	✓	✓	✓	✓
	4	n/a	No text file available.		✓	✓	~	~	~	✓
	5	1	12-07 05:40:52.18	12-07 05:41:58.76	✓	✓	✓	✓	✓	✓
12-08	1	1	12-08 03:40:37.56	12-08 03:41:44.14	✓	✓	✓	✓	✓	✓
	2	60	12-08 03:44:23.19	12-08 04:44:29.24	✓	✓	✓	✓	✓	✓
	3	1	12-08 04:52:10.51	12-08 04:53:17.10	✓	✓	✓	✓	✓	✓
	4	60	12-08 04:57:24.83	12-08 05:19:34.28	✓	✓	~	✓	~	~
	5	1	12-08 06:00:56.20	12-08 06:02:02.83	✓	✓	✓	✓	✓	✓
	6	30	12-08 06:03:35.39	12-08 06:33:41.51	✓	✓	✓	✓	✓	✓

* The filenames for this date in the repository erroneously give the date in yymmdd format as 231124 (rather than 231123). PG02 data collected prior to this date were collected from the antenna being 0.20 m higher than shown in Fig. 6.

~ Video file exists, but may be corrupted.

https://doi.org/10.5194/egusphere-2026-5057
Preprint. Discussion started: 8 September 2026
© Author(s) 2026. CC BY 4.0 License.

Table 3. SITE CONFIGURATIONS FOR DATA COLLECTION

Parameter	Phoenix	Pegasus
Site ID of D_0	PX10	PG10
D_0 ITRF2020 Latitude	-77°, 56', 53.17699"	-77°, 57', 23.74293"
D_0 ITRF2020 Longitude	166°, 44', 41.28355"	166°, 30', 7.28000"
D_0 ITRF2020 Ellipsoidal height	-33.449 m	-38.484 m
GNSS positioning make/model	Trimble NetR8	PG10: Trimble NetR8
GNSS positioning antenna	Trimble Zephyr GNSS Geodetic II	Trimble Zephyr GNSS Geodetic II
Site ID of I_0	PHNX	PG02
I_0 ITRF2020 Latitude	-77°, 56' 52.72136"	-77°, 57', 23.64336"
I_0 ITRF2020 Longitude	166°, 44', 41.24918"	166°, 30', 9.48309"
I_0 ITRF2020 Ellipsoidal height	-41.124 m	-46.211 m
GNSS-IR make/model	PHNX: Septentrio PolarX5	PG02: Trimble NetR9
GNSS-IR antenna	Septentrio PolaNt-x MF	Trimble Zephyr GNSS Geodetic II
Site name of R_0	PHNX-R	PGSS-R
USRP make/model	Ettus N210	Ettus N210
Clock used	Ettus GPS-disciplined oscillator	Ettus GPS-disciplined oscillator
Reflectometry antenna	Antcom G8Ant-3A4TB1-LH Rev A	G8Ant-3A4TB1-LH Rev A
USRP sampling rate	5 MHz complex	5 MHz complex
reflected USRP inline gain (dB)	40	40
reflected USRP RF gain (dB)	31	31
Lidar make/model	Velodyne VLP-16	Ouster OS0-32-Rev-06, Gen2 32 Below Horizon
Camera make/model (x4)	GW 5050 IP Security camera	GW 5050 IP Security camera
azimuth angle of the boom, $\mu = \tan^{-1}(\boldsymbol{r}^{I_0/D_0})$	-0.91°	77.75°
Relative heading angle μ_1, μ_5 of cameras 5 and 1	$(60+3)°$	(246-8)°
Relative heading angle μ_2, μ_6 of cameras 6 and 2	$(180-58+4)°$	(69+8)°
Relative heading angle μ_3, μ_7 of cameras 7 and 3	295°	(0-2)°
Relative heading angle μ_4, μ_8 of cameras 8 and 4	$0+4.3°$	(310+4)°
Elevation angle κ of reflected antenna	-90°	-90°
Elevation angle of lidar ψ_L	0°	0°
Elevation angle ψ_1, ψ_5 of cameras 5 and 1	$(-18+5)°$	(-17+0)°
Elevation angle ψ_2, ψ_6 of cameras 6 and 2	$(-18+4.5)°$	(-13+0)°
Elevation angle ψ_3, ψ_7 of cameras 7 and 3	$(-17+0)°$	(-16+5.5)°
Elevation angle ψ_4, ψ_8 of cameras 8 and 4	$-(18+9.7)°$	(-17+4.5)°
$\boldsymbol{r}^{D_0/R_0}$ in $\left[\hat{t}, \hat{b}, \hat{u}\right]$ m	$[0, 0.07, 0.51]$	$[0, 0.07, 0.48]$
$\boldsymbol{r}^{R_0/L_0}$ in $\left[\hat{t}, \hat{b}, \hat{u}\right]$ m	$[0, -0.34, 8.31]$	$[0, -0.53, 6.38]$
$\boldsymbol{r}^{L_0/C_{0,8}}$ and $\boldsymbol{r}^{L_0/C_{0,3}}$ in $\left[\hat{t}, \hat{b}, \hat{u}\right]$ m	$[0, -0.05, -1.37]$	$[0, 0.21, 0.49]$
$\boldsymbol{r}^{C_{0,6}/C_{0,8}}$ and $\boldsymbol{r}^{C_{0,1}/C_{0,3}}$ in $\left[\hat{t}, \hat{b}, \hat{u}\right]$ m	$[0, -1.22, 0]$	$[0, -1.31, 0]$
$\boldsymbol{r}^{C_{0,5}/C_{0,8}}$ and $\boldsymbol{r}^{C_{0,2}/C_{0,3}}$ in $\left[\hat{t}, \hat{b}, \hat{u}\right]$ m	$[0.61, -0.61, 0]$	$[0.42, -0.62, 0]$
$\boldsymbol{r}^{L_0/C_{0,7}}$ and $\boldsymbol{r}^{C_{0,4}/C_{0,3}}$ in $\left[\hat{t}, \hat{b}, \hat{u}\right]$ m	$[0.61, 1.78, -0.15]$	$[-0.89, -0.62, 0]$
Cameras 5 and 1 HFOV, VFOV	$73.470°, 44.760°$	$78.945°, 49.711°$